MINISTERE DE L'ENSEIGNEMENT SUPERIEUR ET DE LA RECHERCHE SCIENTIFIQUE

Felix Houphouet-Boigny university

UNITE DE FORMATION ET DE RECHERCHE SCIENCES DES STRUCTURES DE LA MATIERE ET DE TECHNOLOGIE

RÉPUBLIQUE DE CÔTE D'IVOIRE
UNION - DISCIPLINE - TRAVAIL

Forschungzentrum Jülich

N°: 662

SPONSORED BY THE Federal Ministry of Education and Research

MASTER

IN RENEWABLE ENERGY AND CLIMATE CHANGE

SPECIALITY: PRODUCTION AND TECHNOLOGY OF GREEN HYDROGEN

MASTER THESIS:

Subject/Topic:

SALT-WATER ELECTROLYSIS FOR GREEN HYDROGEN ECONOMY

Presented on the 26th of Septembre 2023 by

Bintou Issa DEMBELE

Jury:

Prof. OBROU Olivier	**President**
Dr (MC) N'GUESSAN Alexandre	**Examiner**
Dr. KOFFI Aka Stéphane	**Major-supervisor**
Prof. Dr. Rüdiger A. EICHEL	**Co-supervisor**

Academic year: 2022-2023

FORWARD AND ACKNOLEDGEMENT

I would like to acknowledge and express my sincere gratitude to the following individuals and organizations who have played instrumental roles in shaping my educational journey and academic success:

I am deeply appreciative of the support provided by the BMBF and Wascal for awarding me the scholarship that made my educational pursuits possible.

I extend my thank to the president of the University Abdoul Moumouni Prof. Mamadou Saidou, to the president of the University Felix Houphouet Boigny Ballo Zie where I have received my certificate. I am grateful to the vice chancellor of forschungszentrum Julich and the director of the institute IEK-9 (Fundamental electrochemistry), where I completed my internship. My Thanks to the team members of Wascal Côte D'Ivoire.

I am deeply indebted to my Co-Supervisor Prof. Dr. Rüdiger A. Eichel for their consistent support, expertise, and guidance throughout my academic pursuits.

I extend my thanks to my Major-Supervisor Dr Koffi Aka Stéphane for their valuable insights and contributions that have enhanced the quality of my academic work. I would like to acknowledge the jury president Prof. OBROU Olivier and the jury examiner Dr. (MC) N'GUESSAN Alexandre for their valuable time, expertise, and evaluation of my academic achievements.

Thank you to the team members from Niger who were involved in both the first and second semesters of my academic journey, for their collaboration and support. I am particularly grateful to my parents, Issa Dembele and Kadidia Traore and my brother Boubacar Issa Dembele, who have been nothing but supportive and caring throughout my entire life. I feel very lucky to be surrounded by such loving family members: Savadogo's family, Rokiatou Mamadou Diallo, Aiché Diallo, Moussa Diakité, Manthia Fofana, Mabintou Tangara, Adam Sidibe, Kadidia Hatallaya.

I can't end these acknowledgments without mentioning the best daily supervisors Jan Uecker and Dr. Lucy Nohl. My heartfelt gratitude for their exceptional leadership and guidance as my supervisors, and for the work atmosphere that they have created during my stay. Thank you to all the team members of IEK-9.

ABSTRACT

In this study, we investigate effects of seawater electrolysis on the performance and durability of solid oxide electrolysis cells, with a focus on their short-term stability and operational efficiency. The abundant and easily accessible nature of seawater offers an enticing potential to bolster the sustainability of hydrogen production processes using solid oxide electrolysis cell (SOEC) technology. To assess the impact of seawater electrolysis, a comprehensive experimental investigation was conducted using fuel electrode single supported cell Ni-YSZ/YSZ/LSCF-GDC. The experimental parameters included temperature variation, steam concentration variation and short-term durability. The effect of seawater on the performance of solid oxide electrolysis cells (SOEC) were examined by electrochemical characterization and impedance analysis. Our findings reveal that increasing the temperature of the cell leads to a good performance of electrolysis. Increasing the H_2O content could also improve the electrolysis efficiency. Furthermore, the study examines the short-term degradation of SOECs at different temperatures and different steam concentration. The results show that the highest degradation rate at different steam concentration is occurring at 50% with a degradation rate of 1 $A \cdot cm^{-2}$/ h. At different temperatures, the highest degradation rate is observed at 750^{o}C.

Keywords: Seawater; Solid oxide electrolysis cell; Hydrogen economy; steam concentration; temperature variation; Short-term degradation.

RESUME

Dans cette étude, nous examinons les effets de l'électrolyse de l'eau de mer sur les performances et la durabilité des cellules d'électrolyse à oxyde solide, en mettant l'accent sur leur stabilité à court terme et leur efficacité opérationnelle. La nature abondante et facilement accessible de l'eau de mer offre un potentiel attrayant pour renforcer la durabilité des processus de production d'hydrogène en utilisant la technologie des cellules d'électrolyse à oxyde solide (SOEC). Pour évaluer l'impact de l'électrolyse de l'eau de mer, une enquête expérimentale approfondie a été menée en utilisant une cellule à électrode de carburant unique avec support, connue sous le nom de Ni-YSZ/YSZ/LSCF-GDC. Les paramètres expérimentaux comprenaient des variations de température, des changements de concentration de vapeur et l'évaluation de la durabilité à court terme. L'effet de l'eau de mer sur les performances des cellules d'électrolyse à oxyde solide (SOEC) a été examiné par caractérisation électrochimique et analyse d'impédance. Nos découvertes révèlent que l'augmentation de la température de la cellule conduit à de meilleures performances d'électrolyse. L'augmentation de la teneur en H2O pourrait également améliorer l'efficacité de l'électrolyse. De plus, l'étude examine la dégradation à court terme des SOEC à différentes températures et concentrations de vapeur. Les résultats montrent que le taux de dégradation le plus élevé à différentes concentrations de vapeur se produit à 50 %, avec un taux de dégradation de 1 A·cm-2/h. À différentes températures, le taux de dégradation le plus élevé est observé à 750°C.

Mots-clés : Eau de mer ; Cellule d'électrolyse à oxyde solide ; Économie d'hydrogène ; Concentration de vapeur ; Variation de température ; Dégradation à court terme.

TABLE OF CONTENT

LIST OF FIGURES:

LIST OF TABLES:

LIST OF ABBREVIATIONS:

ρ: Partial Pressure (bar)

σ_0: Conductance (S)

8YSZ: 8% mol Yttrium stabilized zirconia

AC: Alternative current

ASR: Area specific resistance

CPE: constant phase element

DC: direct circuit

DRT: Distribution of Relaxation Times

Ea: Activation Energy ($J \cdot mol^{-1}$)

E_{cell}: Cell Potential (V)

ECM: equivalent circuit models

EIS: Electrochemical Impedance Spectroscopy

GDC: gadolinium-doped ceria

H_2: Hydrogen

H_2O: Water

H_2S: hydrogen sulfide

HCl: hydrogen chloride

IEA: International Energy Agency

IV-curve: Current-voltage curve

LSC: Lanthanum strontium cobaltite

LSCF: Lanthanum-strontium cobalt ferrite

LSM: strontium doped lanthanum manganite

N_2: Nitrogen

Ni: Nickel

NiS: Nickel sulfide

NZE: zero emission scenario

O_2: Oxygen

OCV: open circuit voltage

OER: Oxygen enhancement ratio

PEFC: Polymer electrolyte fuel cell

PV: photo-voltaic

R_p: Polarization resistance

R_Ω: ohmic resistance

SEM: Scanning electron microscopy

SO2: Sulfur dioxide

SOEC: Solid oxide electrolysis cell

SOFC: Solid oxide fuel cell

$SrCrO_4$: Strontium chromate

T: Temperature (K)

t: Time (s)

TBP: Triple boundary phases

TEC: Thermal expansion coefficient

Z: Impedance (Ω)

ΔG: Gibbs' free energy change

η: Overpotential (V)

τ: Time Constant (s)

Φ: Phase Shift (rad)

ω: Radial Frequency ($rad \cdot s^{-1}$)

GENERAL INTRODUCTION

GENERAL INTRODUCTION

Fossil fuels have been the backbone of energy systems for centuries. The burning of fossil fuel release carbon dioxide (CO_2) and other greenhouse gases into the atmosphere. According to Kaur et al. fossil fuels release around 36 gigatons of CO_2 every year, leading to greenhouse effects and causing climate change and earth's temperature to rise [1]. Nowadays, climate change is one of the main issues for all governments around the world that they want to fix. It is vital to research and use clean and renewable energy sources in order to reduce this issue [2].

According to the International Energy Agency's (IEA) World Energy Outlook 2021, there will be a significant shift in the energy sector from fossil fuels to renewables by the year 2050. In a net zero emission scenario (NZE), it is predicted that about 90% of the world's electricity will be produced by renewably generated energy, with wind and solar photo-voltaic (PV) accounting for 70% of that total (90%) [3]. However, solar and wind energy are both dependent on specific environmental conditions and their generation can be affected by seasonal variation. Furthermore, the year-round availability of hydropower is inconsistent. While biomass is a renewable energy source that maintains a steady supply, it falls short in meeting the global energy demands due to the significant requirement of fertile land for food production [4].

Hydrogen has received more attention recently as a potential alternative energy source for a post-carbon economy. The cleanest way to create hydrogen from electricity is probably water electrolysis. The utilization of energy systems that combine electrolysers with intermittent renewable energy sources, like solar or wind, will increase in the near future to store electrical energy as chemical energy, for example in the form of hydrogen, syngas, etc.

Vast quantities of water are needed for large-scale electrolysis of water in order to produce hydrogen. To produce only 1 kg of H_2, 9 liters of water are required. According to the United Nations'2018 world water resources development report, approximately 3.6 billion people worldwide reside in areas with water deficit. This figure is projected to increase to somewhere between 4.8 and 5.7 billion by 2050, indicating that the existing freshwater supply will be insufficient for human consumption [5]. As a result, the electrolysis technique, which relies on freshwater or pure water as its primary input, maybe adversely affect the future. However, sea water sources remain abundant (96.5%) [6], easily accessible, and untapped offering great potential [5].

Alkaline electrolysis, proton exchange membrane electrolysis, anion exchange membrane electrolysis, high temperature solid oxide electrolysis cell (SOEC), and others are the main water electrolysis technologies. Alkaline electrolysis and proton exchange membrane electrolysis are relatively developed and marketable, but they still face certain difficulties when splitting seawater [5]. Seawater compositions contain more, and different contaminants compared to freshwater. These impurities and often toxic ions might erode the electrolyzer and obstruct the water decomposition reaction [5]. High temperature SOEC offers a solution to numerous challenges encountered during room temperature seawater electrolysis due to the need to evaporate the used water. Most of the salt remains solved in the liquid phase.

High-temperature electrolysis of steam using SOECs is a promising technology to produce hydrogen, considering the thermodynamic perspective. This is because it requires less electrical energy per unit of hydrogen produced compared to low-temperature water electrolysis. Moreover, the kinetics at high temperatures are improved [7].

In this work, SOEC is used to split seawater into hydrogen, and the electrochemical characterization of the SOEC with a gas composition of 40 % H_2O and 60 % H_2 is investigated. The SOEC's response to the possible degradation caused by seawater is examined at various steam compositions and temperatures. Long-term stability of solid oxide electrolyzes cells at a given temperature is investigated in addition.

The introduction to an overview of green hydrogen economy, SOEC’s and the seawater in this thesis report comes first. The principle of high temperature electrolysis cell and the influence of contaminants in SOEC operations are thoroughly described in Chapter one, with an emphasis on the SOEC components and materials, and electrochemical methods. The tools and procedures utilized for the analysis are outlined in chapter two. The investigation's findings are presented in chapter three along with a discussion of them. Chapter four concludes with an overview of the thesis' findings and a brief recommendation.

CHAPTER I: LITTERATURE REVIEW

CHAPTER I: LITERATURE REVIEW

Introduction

This chapter consists of an overview of the principles, materials and components of the SOEC technology. It further describes the influence of contaminants in SOEC operation and concludes with the electrochemical methods.

1. Description of the high temperature electrolysis cell

1.1. Work principle

The SOEC is an electrochemical device that operates in reverse mode of the solid oxide fuel cell (SOFC). While an SOFC generates electricity from fuel, an SOEC utilizes electricity to power an electrolysis process that produces hydrogen or other gases [8].

Figure 1 shows a schematic representation of a SOFC and SOEC cell in the case of a H_2O/H_2 system. During the electrolysis process, when a sufficiently high electrical potential difference is applied across the electrolyte, the oxygen ions (O^{2-}) are driven from the cathode to the anode through the electrolyte. The reactions taking place in a SOC can be divided into half-cell reactions [9]. At the cathode, water molecules combine with electrons from the external circuit and undergo dissociation, resulting in the formation of hydrogen and oxygen ions (equation 1). At the anode, oxygen gas (O_2) is produced (equation 2). The produced oxygen gas can be collected at the anode side, while the other desired gases, such as hydrogen (H_2), can be collected at the cathode side [10].

$$\boldsymbol{H_2O + 2e^- \Leftrightarrow O^{2-} + H_2} \quad \textbf{(1)}$$

$$\boldsymbol{O^{2-} \Leftrightarrow 0.5O_2 + 2e^-} \quad \textbf{(2)}$$

The electrode where reaction (1) takes place is always the same, although it is referred to as the cathode when using an electrolysis device and the anode when operating a fuel cell. The electrode where reaction (1) occurs is always referred to as the H_2- electrode, whereas the electrode where reaction (2) occurs is referred to as the O_2-electrode. This is done to avoid any mistakes [11].

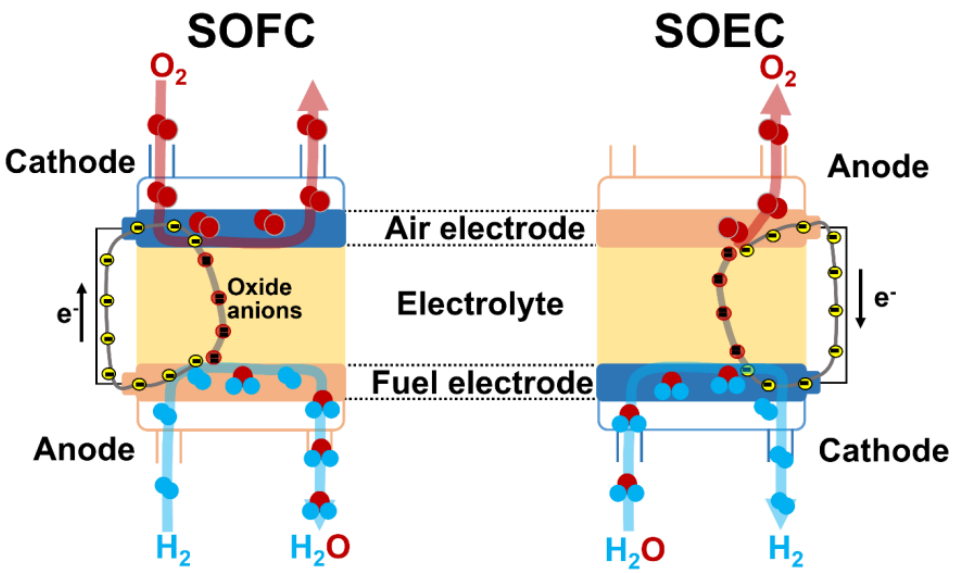

Figure 1: A schematic representation of the operating principle of a SOFC (left) and SOEC (right) for H_2O/H_2 operation.

The standard SOEC operates at high temperatures between 650 °C and 950 °C due to the requirement of high temperature for the ionic conduction of oxide ions through solid ceramic electrolyte. It is only at high temperature that the oxide ions are mobile. Solid oxide electrolysis is performed using ceramic cells equipped with a solid electrolyte and ceramic, metal or cermet electrodes. The unique aspect of SOEC is the presence of a solid, ion-conducting electrolyte [10].

The SOEC electrodes need to be very porous in order to facilitate gas diffusion. To allow efficient electron transfer across the electrodes, minimizing energy losses, the electrode must have high electrical conductivity. High ionic conductivity is required in the electrode and electrolyte in order to enable rapid ion diffusion, reducing the resistance of ion flow and allowing for faster electrochemical reaction. Efficient and sustainable conversion of water into valuable products in SOECs requires strong electrocatalytic activity of the electrode. Faster reaction kinetics, reduced energy losses, cell stability, and optimized utilization of electrode materials are all crucial factors contributing to the overall performance and viability of the SOEC system [12]. With a high ionic but very low electronic conductivity, the electrolyte must be thick and gas tight in order to prevent the mixing of these gases, ensuring that they are collected separately at the respective electrodes. If the electrolyte was not gas tight, gas crossover could occur, leading to reduced purity and lower efficiency of the produced gases. The chosen materials must be chemically and physically stable,

as well as compatible with each other, i.e. having a similar thermal expansion coefficient (TEC). A mechanical support should also be given if it is not externally provided (such as in a metal-supported cell), so that one electrode or the electrolyte have a sufficient mechanical stability [13].

1.2. Thermodynamics

The process enthalpy change (ΔH), which consists of the entropy term (TΔS) as thermal energy (Q) and the Gibbs' free energy change (ΔG) as electric energy, gives the amount of energy needed for the electrolysis reaction. The relationship between these thermodynamic quantities is given by the following expression [14]:

$$\mathbf{\Delta H = \Delta G + T\Delta S,} \qquad \mathbf{(3)}$$

where ΔH is the change in enthalpy, T is the temperature, and ΔS is the change in entropy. As temperature rises, the electrical energy requirement, ΔG, decreases, while the heat requirement increases (**Fig. 2**).

The electrochemical reaction known as electrolysis is endothermic (ΔH > 0) and nonspontaneous (ΔG> 0). **Figure 2**shows how the energy demand and required cell voltage dependence on the temperature at 0.1 MPa steam pressure. In this graph, it can be seen that ΔG declines and heat energy demand(TΔS) grows with increasing temperature, which is financially beneficial, as over two thirds of the cost of electrolytic hydrogen comes from the usage of electricity. Even though the total energy demand is rising slightly, the decline in electrical energy demand is more significant. If the increase in heat energy demand can be fulfilled by an external heat source, such as nuclear power, renewable energy, or waste heat from high-temperature industrial processes, operating at higher temperatures can decrease the cost of the hydrogen produced [15].

The minimum cell voltage (or reversible cell voltage) Vr necessary for the electrolysis reaction to occur is expressed as the Gibbs' free energy change (ΔG) from a thermodynamic perspective as follows [14]:

$$\boldsymbol{Vr = \frac{-\Delta G}{n \cdot F}} \qquad \mathbf{(4)}$$

where n is the number of moles of electrons per mole of products and F is the Faraday constant, 96 485 $C.mol^{-1}$.

The minimal voltage required for electrolysis to take place if the heat energy TΔS is supplied by electricity, is known as the thermo-neutral voltage (V_{tn}), which is the situation in the majority of commercial electrolysers.

$$V_{tn} = \frac{\Delta H}{n \cdot F} \quad (5)$$

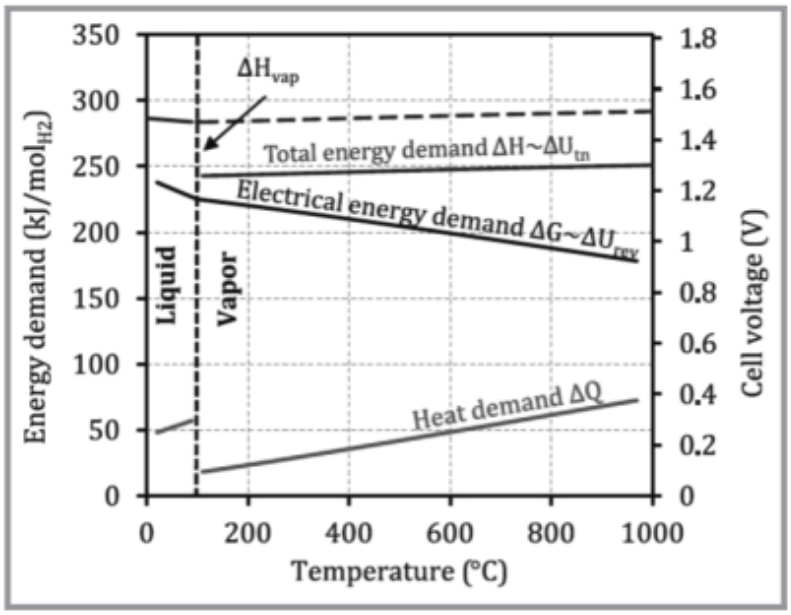

Figure 2: Energy demand and cell voltage with respect to temperature for water/steam electrolysis with 0.1 MPa steam pressure [16]

2. Materials and component of SOEC

The electrolysis electrochemical devices are made up of two electrodes (anode and cathode) and an electrolyte at their most basic level [17].

2.1. Electrolyte

The surrounding layers of the SOEC, including the hydrogen electrode, oxygen electrode, are influenced by the electrolyte, which is positioned at the core. In order to enable optimal performance, the electrolyte should exhibit high ionic conductivity, for example O^{2-}oxygen ions. Additionally, the electrolyte must possess electrical insulating properties to prevent short circuits and be adequately dense to prevent gas transport between the atmospheres of the two electrodes. The required density can be reached by proper sintering [15,18].

Ensuring sufficient durability requires critical mechanical strength, thermal stability, and chemical stability of the material. The leading material in this regard is 8 mol% yttria-doped zirconia (8YSZ), which is a dense ceramic composed of zirconium oxide. Yttria addition stabilizes its cubic crystal structure. Based on its high ionic conductivity (10^{-2}– 10^{-1} S cm^{-1}) and excellent thermal and chemical stabilities, 8YSZ exhibits good and consistent performance within the typical temperature range of 700–850°C in SOECs. Another electrolyte material gaining interest is gadolinium-doped ceria (CGO or GDC), mainly due to its high ionic conductivity. However, the challenge lies in its high sintering temperature of approximately 1500°C, which limits the options for co-sintering [18].

2.2. Fuel electrode/hydrogen electrode

The triple phase boundaries, also known as TPB, are locations where the electrical phase (electron conductive nickel Ni), the ionic phase (O^{2-} conductive YSZ), and the gaseous phase (steam supply and hydrogen release) intersect. These locations are within 5 to 10 micrometers(um) of the electrolyte/electrode contact. As a result, the hydrogen electrode material must be a porous electronic-ionic conductor. The most advanced substance is a ceramic-metal (cermet) compound made of Ni, a non-precious metal catalyst with high electronic conductivity, and YSZ, providing high ionic conductivity [18].

However, Ni-YSZ cermet are facing some challenges during long-term operation under electrolysis mode. Microstructural deformation resulting from Ni-migration and Ni-coarsening, which has been identified as a significant factor is one of the causes of the degradation of the Ni-YSZ electrode. To minimize the Ni-migration, various techniques for microstructural optimization have been implemented [19], such as the infiltration of GDC nanoparticles into the Ni-YSZ cermet. Ovtar et al. [19] report a significant decrease of voltage degradation of 633 mV/kh from 699 mV/kh for Ni-YSZ to 66 mV/kh for GDC-infiltrated Ni-YSZ, which is surpassing a reduction of 90% [20].

2.3. Air electrode/O_2 electrode

The oxygen electrode, also known as the O_2 electrode is responsible for the oxidation of O^{2-} ions into oxygen, primarily in the initial microns near to the interface of the electrode and electrolyte. For a material to be considered suitable, it needs to possess high mixed ionic-electronic

conductivity, excellent electrocatalytic activity, and should be chemically and thermally compatible with the electrolyte over an extended period. Achieving this last requirement is particularly challenging. As a result, an intermediate layer is typically necessary between the oxygen electrode and electrolyte [15].

Due to its excellent long-term stability, good catalytic properties at high operating temperatures, strontium doped lanthanum manganite (LSM)- yttria stabilized zirconia (YSZ) composite has found extensive application in SOEC as an air electrode. LSM exhibits a high level of electronic conductivity and possesses a thermal expansion coefficient (TEC) that closely matches that of the electrolyte [21]. LSM and YSZ are also chemically compatible and have little chemical reactivity. In the composite, YSZ serves as the structural element and offers ionic conduction, while LSM performs catalytic and electronic conduction.

Lanthanum-strontium cobalt ferrite (LSCF) or lanthanum-strontium cobaltite (LSC) are examples of mixed conductors that can be also used as air electrode in SOEC. Fast oxygen ion and electron conduction is possible with the mixed ionic-electronic conductor known as LSCF. It serves as an extremely effective catalyst for oxygen reduction and evolution reactions. In some systems, the electrolyte and the LSCF cathode are separated by a buffer layer (0.1 to 5 um) made of GDC to prevent a reaction between the oxygen electrode materials and YSZ [22].

3. The influence of contaminants in SOEC operation

3.1. Sulfur

In SOEC various sulfur compounds can be encountered depending on the composition of the feedstock and the operating condition. One common sulfur compound that can occur in certain feedstocks is hydrogen sulfide (H_2S). H_2S is corrosive and can have several consequences on the fuel gas electrode and overall cell performance. In the presence of H_2S, Ni-YSZ electrode degrades by forming nickel sulfide (NiS). This sulfidation process can cause the reduction of the TPB where active ionic species transfer at the gas/electrode/electrolyte interfaces [23].

Sulfur chemisorption on the electrode and electrode saturation can cause degradation, resulting in a reduction of active sites. The oxidization of Ni under these poisoning conditions has been observed, leading to increased polarization and a significant increase in cell voltage, ultimately diminishing the effectiveness of the nickel catalyst [24].

Other sulfur impurities, particularly in the form of sulfur dioxide (SO_2), can impact the anode materials in SOECs. Common anode materials include perovskite oxides like LSM or LSCF. Research and approaches have been undertaken to prevent sulfurous contamination of the cell due to the formation of $SrSO_4$ deposits on the electrode surface at the LSCF air electrode. These deposits occur whenSO_2 impurities in the gas react with strontium, ultimately hindering oxygen diffusion [8].

3.2. Chromium

Chromium is another contaminant, which can affect the SOEC anode. It comes from chromium-containing ferritic steels which is used for interconnects and balance of plant (BOP) components. The air electrode is affected by chromium species that diffuse through the TPB or as gaseous $CrO_2(OH)_2$ species (equation 6), limiting the oxygen reduction reaction [8].

In the presence of strontium and manganese such as in the LSM cathode, gaseous chromium can react with them by forming solid $SrCrO_4$ and spinel-type $(Cr, Mn)_3O_4$which can reduce the electrochemical activity by accumulating on the TPB. Research has shown that chromium deposition occurs on the electrode (LSCF) or the electrolyte surface (LSM-YSZ), depending on the materials of the cell. This deposition significantly reduces the cell efficiency by obstructing the active area for oxygen reduction or oxide oxidation at the interphase between the electrolyte and electrode [8].

In SOEC, when chromium is exposed to humid air, it can form various compounds depending on the condition. One the compounds that can be formed is $CrO_2(OH)_2$, the most abundant gaseous chromium. The following reaction shows how the gaseous species is formed:

$$\mathbf{Cr_2O_3}(s) + \frac{3}{2}\boldsymbol{O_2}(g) + 2\boldsymbol{H_2O}\ (g) \leftrightarrow 2\boldsymbol{CrO_2}\ (\boldsymbol{OH})_2\ (g) \qquad \textbf{(6)}$$

This species undergoes reduction at the TPB, leading to the formation of solid Cr_2O_3. Consequently, the active area at the boundary is reduced, impeding the process of oxygen reduction, and causing electrode poisoning.

3.3. Silicon

The separation of gaseous species and leak-proof stacks are crucial for efficient operation in various SOFC/SOEC systems. To achieve this, glass sealants are used to hermetically seal cell

stacks. However, a consequence of this sealing process is the introduction of silicon impurities. In SOFC and SOEC systems with steam, volatile silicon species ($Si(OH)_4$) can form from the glass sealants and deposit as silica (SiO_2) at the active TPB sites of the Ni-YSZ electrode/YSZ electrolyte interface. This blocks the electrocatalytic sites and increases the fuel electrode's non-ohmic polarization and ohmic losses. The deposition of solid SiO_2 occurs as a result of the following equation [8]:

$$\boldsymbol{Si(OH)_4(g) \leftrightarrow SiO_2(s) + 2H_2O\ (g)} \quad \textbf{(7)}$$

3.4. Chlorine compounds

The presence of chlorine compounds has been observed to have negative effect on the Ni-YSZ electrode when used in fuel cell mode. The primary chlorine compound which has been studied is hydrogen chloride (HCl). HCl is a common impurity in fuel gas streams [25].

In their study, Trembly et al. [26] investigated the impact of HCl on the Ni-YSZ anode in electrolyte-supported cells. They subjected the cells to syngas containing 20 and 160 ppm(v) HCl and observed a significant degradation in cell performance. After 100 hours, the performance degradation reached approximately 17% and 26% for the respective HCl concentrations. The researchers attributed this degradation to the formation of nickel chloride, which was found to be unstable based on the observed reversibility of the HCl-induced poisoning. Additionally, they proposed that the adsorption of chlorine onto Ni, leading to a reduction in the active TPB, could provide an alternative explanation.

With time, the cell performance degrades due to a continuous process in which the adsorption of chlorine onto Ni surfaces blocks potential reaction sites at the TPB. This blockage hinders the electrochemical reaction and results in an increase in anode overpotential [26].

3.5. Seawater's contaminants

There are various contaminants in seawater, such as metal ions from various salts, organic pollutants etc. It was shown that the maximum reported concentration belongs to organic pollutants and this can reduce the efficiency of the cell and decrease the overall performance [27].

The salts could interfere with water electrolysis by taking part in different competing electrochemical reactions to hydrogen evolution reaction (HER) at the cathode by transport in the

steam and deposit of solid on the electrode. Furthermore, the existence of bacteria and microscopic organisms in naturel seawater can also result in the creation of solid deposits on the active region of the catalyst's surface. These deposits have a potential impact on the performance of the HER [28-30].

Competitive oxidation of chloride ions in seawater decreases the OER's effectiveness while also creating chlorine-containing species that harm the electrolysers and have negative environmental effects [31].

4. Electrochemical Methods

4.1. Polarization losses

When current is drawn (SOFC) or applied (SOEC), the cell voltage will decrease or increase, respectively. The deviation between the real cell voltage and the Nernst voltage is caused by the polarization loss of the cell. However, it is important to note that the Nernst voltage of the inlet composition can only be achieved when there is no current flowing through the circuit. The Nernst voltage is the theoretical voltage based on thermodynamics. In fuel cell mode, it is the theoretical maximum voltage that can be reached, in electrolysis it is the theoretical minimum voltage that is needed for a reaction to occur. **Figure 3** depicts the typical polarization curves for Polymer electrolyte fuel cell (PEFC) and SOFC, in which three domains can be distinguished: the activation polarization, the ohmic polarization and the diffusion polarization.

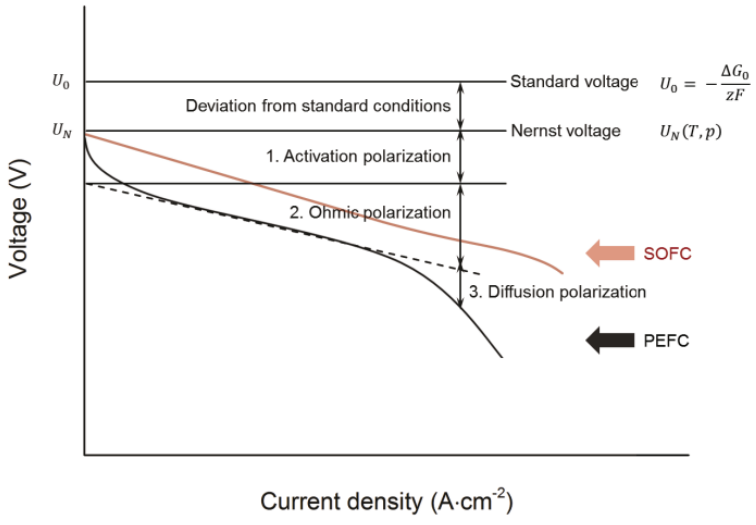

Figure 3: Typical polarization curves (voltage vs. current density) of fuel cells [32].

The activation polarization η_{act} is the first non-linear curve to arise at low current density. This defines the additional voltage needed to overcome the energy barrier involved in the electrochemical processes. The Butler-Volmer equation (Eq. 8) can be used to describe the effect of activation overpotential on current density for each individual electrode [32]:

$$\boldsymbol{j = j_0 \cdot \left[\exp\left(\frac{\alpha_a z F \eta}{RT}\right) - \exp\left(-\frac{\alpha_a z F \eta}{RT}\right)\right]} \quad \textbf{(8)}$$

In where z is the number of electrons involved in the electrode reaction,j_0 is the electrode exchange current density,α_a is the anodic charge transfer coefficient,α_c is the cathodic charge transfer coefficientand η is the activation overpotential.

At medium current densities, the polarization curve appears linear. The polarization in this region is also known as the ohmic polarization (η_{ohm}) because the linear potential decrease in this zone complies with Ohm's law. Ohmic polarization refers to the voltage drop or increase that occurs across the electrolyte material due to its inherent resistance to the flow of electric current. When an electric current passes through the solid electrolyte material in an SOEC, the ions within the electrolyte experience resistance to their movement. This resistance leads to a voltage increase along the electrolyte, which can be described as ohmic polarization. It is possible to express the ohmic polarization, which is the result of electronic and ionic transport in the electrodes and electrolyte, as follows [32]:

$$\boldsymbol{\eta_{ohm} = j \cdot \sum_i R_i = i \cdot R_{tot}} \quad \textbf{(9)}$$

At high current density, the cell experiences diffusion polarization (η_{diff}), characterized by an increased voltage. The fuel usage rate rises as the current density increases. When a fuel cell operates with a constant gas supply, gas diffusion becomes limited at high current density, potentially resulting in the depletion of gas at the reaction sites. Meanwhile, the generated hydrogen cannot be effectively removed in a timely manner.

The SOFC operates at a far greater temperature than the PEFC does, which improves the exchange current density and reduces activation polarization. As a result, the polarization curve of the SOFC often does not show the activation polarization zone, as shown in **figure 3** [32].

4.1.1. Open circuit voltage

A voltage known as open circuit voltage (OCV) can be measured when there is no current flowing through the cell. The equilibrium potential or reversible voltage specified in equation (4) is theoretically equivalent to this potential. When using steam, carbon dioxide, or co-electrolysis, the Nernst equation (equation (10)), which is created by substituting equation (11) for equation (4), can be used to compute the OCV for any given gas mixture [10].

$$E_{Nernst} = E^0 - \frac{RT}{nF} ln \prod_{i=1}^{k} {a_i}^{v_i} \quad (10)$$

$$\Delta G = \Delta G^0 + \frac{RT}{nF} ln \prod_{i=1}^{k} {a_i}^{v_i} \quad (11)$$

In these equations, a_i stands for the species activity, i and v_i for the stoichiometric coefficient. The partial pressure p_i can take the place of the activity for gas mixtures, assuming ideal gasses.

When I = 0, it is possible to read the OCV from an IV curve.

4.1.2. Area specific resistance

An electrolysis cell's area specific resistance (ASR) is calculated by multiplying the cell's total resistance by its active area. If the current density is shown instead of the current in an IV curve, the ASR represents the slope of the curve. Either numerical differentiation or fitting a linear function to a brief segment of the IV curve can be used to identify it. If the IV curve is linear across its entire range, equation (11) can be used to get the ASR [10].

$$ASR = \frac{E_{cell} - OCV}{i} \quad (12)$$

4.2. Electrochemical Impedance Spectroscopy (EIS)

In a typical electrochemical cell, in addition to the resistance of the electrolyte, interactions between matter (redox species) and the electrode also involve the concentration of electroactive species, charge-transfer, and mass-transfer from the bulk solution to the electrode surface.

As shown in **Figure 4** [33], an electrical circuit with resistances, capacitors, or constant phase elements connected in parallel or series to create an analogous circuit serves as a symbol for each of these characteristics. Therefore, processes including mass-transfer, charge-transfer, and diffusion could be studied using EIS. As a result, EIS has the capability of researching intrinsic material characteristics or processes that may affect an electrochemical system's conductance, resistance, or capacitance. The difference between impedance and resistance is that the resistance in direct circuit (DC) circuits directly follows Ohm's Law. The impedance response is measured using a modest sinusoidal signal stimulation. The current response to a sinusoidal potential is a sinusoid at the applied frequency. Equation (13) illustrates the excitation signal as a function of time [33]:

$$E_t = E_0 . \sin(\omega t) \quad \textbf{(13)}$$

where $\mathbf{E_t}$ is the potential at time t**,** $\mathbf{E_0}$ is the amplitude of the signal, and **ω** is the pulsation. Equation (14) states the current response with the phase-shift Φ and the amplitude I_0:

$$I_t = I_0 . \sin(\omega t + \phi) \quad \textbf{(14)}$$

Similar to Ohm's law, Equation (15) may be used to determine the impedance Z of the entire system:

$$Z = E/I = Z_0 exp(-i\phi) = Z_0(cos(-\phi) + isin(-\phi)) \quad \textbf{(15)}$$

Equation (16) is used to determine the relationship between the applied frequency (f) and the radial frequency (**ω**):

$$\omega = 2 . \pi . f \quad \textbf{(16)}$$

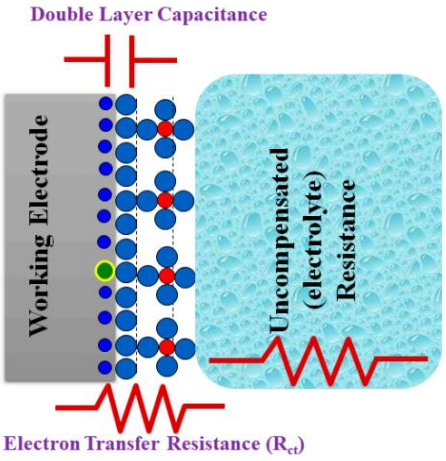

Figure 4: In a typical electrochemical cell (i.e., a three-electrode system), the EIS circuit and the redox reaction occur at the surface of the working electrodes. Charge transfer resistance is denoted by R_{ct}, electrolyte resistance is denoted by R_s, and capacitance double layer is denoted by C_{dl}[33]

A "Lissajous Plot", **Figure 5** (a), is produced when the applied sinusoidal signal is shown on the X-axis and the sinusoidal response signal (I) on the Y-axis. Before the development of contemporary EIS instrumentation, the only method for measuring impedance was Lissajous analysis [34].

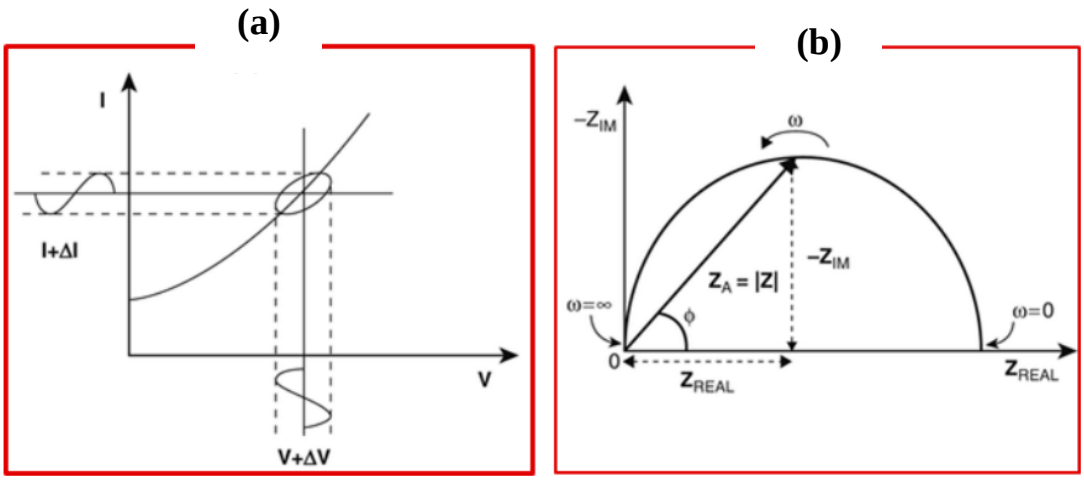

Figure 5: The Lissajous plot (a) and the Nyquist plot vector (b) [33].

There are two parts to the impedance expression: a real part and an imaginary part. A "Nyquist Plot" is created when the imaginary part (Z_{IM}) is plotted on the Y-axis and the real part (Z_{REAL}) is

plotted on the X-axis (**Figure 5**b, right side). The Z_{IM} is negative to represent the data in the first quadrant of a coordinate system. Each point on the Nyquist plot represents an impedance value at a certain frequency. Low frequency impedance is typically on the right side of the plot, whilst higher frequency impedances are on the left. Additionally, impedance can be shown as a vector (arrow) with a length of |Z| on a Nyquist plot. The "phase angle" is the angle formed by this vector and the X-axis [33].

4.2.1. Equivalent circuit models

It is common practice to analyze impedance diagrams using equivalent circuit models (ECM). A measured impedance diagram is fitted using a combination of ideal (resistor, capacitor, inductor, etc.) and non-ideal (constant phase element, or CPE, Warburg, etc.) electrical elements in series and/or parallel. The impedance diagram can be divided into various frequency ranges, each of which is represented by a portion of the ECM [35].

The primary factors governing the system under consideration can be distinguished thanks to the deconvolution of the impedance diagram, with each factor having a frequency range, a relaxation frequency, and electrical element values associated with it [35]. The ECM can then be fitted to the experimental data and should describe all physicochemical processes taking place in the system [10]. Inductors, resistors, and capacitors, as well as constant phase elements, are the most prevalent elements.

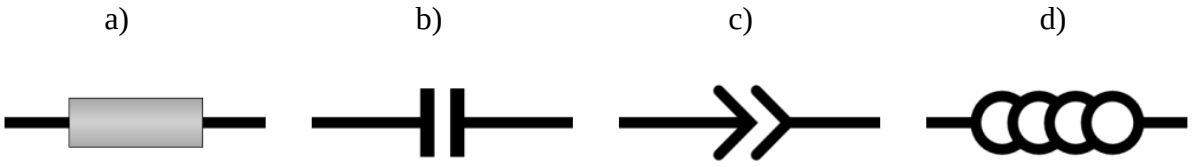

Figure 6:Circuit components are shown schematically as follows:: (a) Resistor, (b) Capacitor, (c) Constant Phase Element, (d) Inductor [10]

4.2.2. Distribution of Relaxation Times (DRT)

The identification of the various processes taking place in the electrochemical system is one of the investigations in EIS. In the Nyquist plot, these distinct processes are shown as arcs.

The quantity of arcs, however, does not necessarily correspond to the total number of distinct processes occurring from the impedance spectra as a whole. The spectrum consists of the arcs from various electrochemical reactions that occur at comparable frequencies overlapping with one another. Therefore, it is impossible to separate such processes from the Nyquist plot [32]. To separate and distinguish such processes, the DRT analysis is employed.

A distribution function of the relaxation periods and amplitudes of impedance-related processes can be calculated directly from experimental data using the deconvolution approach known as DRT. No prior selection of an equivalent electrical circuit model followed by a non-linear least squares curve fit is necessary to obtain these distributions [35]. The DRT method is particularly intriguing because it allows for the elimination of any user subjectivity.

DRT analysis of an impedance diagram can be used as a pre-identification method to choose the ECM that is most suited to the system under study. It is strongly advised to use DRT and ECM together to enhance an objective EIS analysis.

Furthermore, DRT analysis should make it possible to distinguish between the various impedance contributions regardless of the electrochemical configuration (two or three electrodes). This method can result in the separation of anodic and cathodic contributions in the case of SOECs, and notably for cells with thin electrolytes [35].

Conclusion

In this literature review chapter, an exploration of the principles, materials, and components of Solid Oxide Electrolysis Cell (SOEC) technology has been undertaken, along with its operation, thermodynamics, and the critical role played by various contaminants. Emphasis has been placed on the necessity of high-temperature operation and the utilization of suitable materials for electrodes and electrolytes. Furthermore, the impact of contaminants such as sulfur, chromium, silicon, and chlorine on SOEC performance has been discussed, with their potential to degrade electrode materials and hinder overall efficiency being highlighted. The introduction of key electrochemical methods, including Polarization losses, Open Circuit Voltage, Area Specific Resistance, and Electrochemical Impedance Spectroscopy (EIS), has been made, showcasing their significance as essential tools for characterizing and comprehending SOEC behavior. This comprehensive literature review serves as the foundation for further research and development in

the field of SOECs, with a focus on efficiency improvement, durability enhancement, and the promotion of environmental sustainability. The subsequent chapter will delve into the materials and methods used in recent research related to SOEC technology, providing insights into experimental approaches and techniques applied in this field.

CHAPTER II: MATERIAL AND METHODS

CHAPTER II: MATERIAL AND METHODS

Introduction

This chapter provides a detailed explanation of how the study was conducted. The materials and the methods used for the characterization of the SOEC, the durability of the seawater electrolysis and the degradation mechanism for hydrogen production. The software used for the data analysis is also described.

1. Study area

This experimental study has been carried out at IEK-9 (Institute for Energy and Climate Research, Fundamental Electrochemistry) at Forschungszentrum Jülich in Germany.

2. Experimental

For this work, a commercial fuel electrode-supported single button cell from Elcogen® has been used. Ni-YSZ/YSZ/LSCF-GDC is the cell used during the experiments with a total thickness of 315±35 µm and a diameter of 20 mm. **Figure 7** shows the picture of the fresh single button cell which is composed of a LSC ((lanthanum strontium cobaltite) oxygen electrode with thickness of 15 ±5µm (diameter of 10mm), an electrolyte 8YSZ (8 mol% yttria-stabilized zirconia) layer with a thickness ~ 5 µm ,GDC (gadolinium-doped ceria) as a barrier layer between YSZ and LSC (thickness ~2 µm) and the fuel electrode NiO-YSZ (thickness of 300 ±30µm) with an active layer around 10 µm. The active area of the cell was 0.785 cm^2. To more understand the structure of the single cell (**Figure 7**), **Figure 8** shows the scanning electron microscopy (SEM) cross section image of the cell. The seawater used in the electrolysis process was taken from a coastal region in the Netherlands.

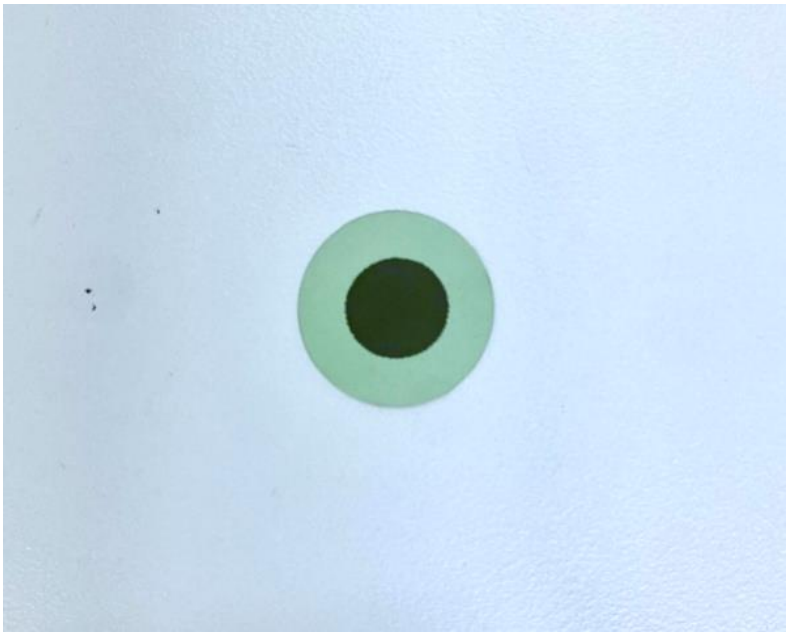

Figure 7: Single button cell of Ni-YSZ/YSZ/LSCF-GDC (Total thickness of 315±35 µm and a diameter of 20 mm)

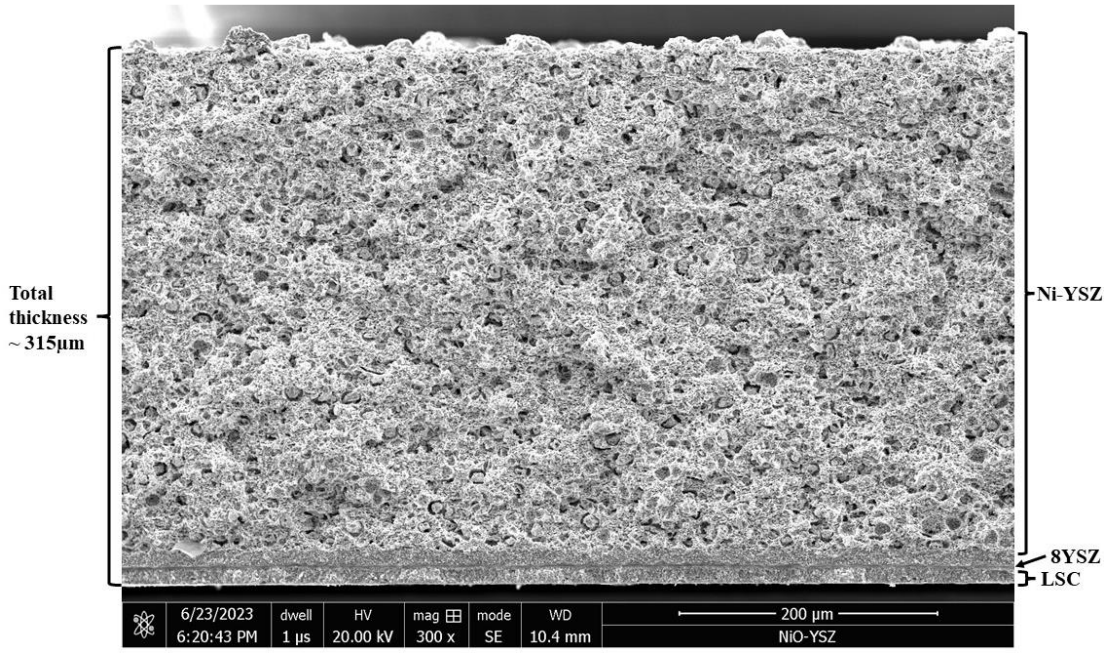

Figure 8: Scanning electron microscopy (SEM) cross section image of the cell

2.1. The reduction and the measurement setup of the single cell

The measurement setup of the single cell is shown schematically in **Figure 9**, the cell was installed in probostat setup (Norwegian Electro Ceramics®, NORECS, Oslo, Norway) with a furnace from the company Carbolite Gero® (Neuhausen, Germany) [36]. A ceramic tube was used where a platin inner current collector was placed (step 1 and 2). A gold ring serving as a gasket to seal the fuel compartment gastight and was positioned between the ceramic holder and the cell (step 3). The cell was mounted onto the gold ring, and the Ni inner current collector contacted the air electrode (step 4). The platin-nickel outer current collector contacted the fuel electrode of the cell (step 5). A compressive force was used to hold the cell in place during the measurement (step 6).

After assembly, the cell is heated to 900°C with a heating rate of 1.5 $°C \cdot min^{-1}$ and a gas composition of 6 $Nl \cdot h^{-1}$ of nitrogen (N_2) at the fuel electrode and 6 $nl \cdot h^{-1}$ of air at the air electrode. The steam/hydrogen electrode's nickel oxide was reduced to Ni after the heat-up process. During the reduction, N_2 and H_2 were used as an inert carrier gas. The use of hydrogen gas is to avoid oxidation of the Ni electrode material. The gas composition of H_2 was gradually raised during the reduction in accordance with Table 1. The gases (H_2, N_2, and air) were controlled by mass flow controllers.

After reducing the cell for 6-7 hours or overnight, a stable open circuit voltage (OCV) is measured. The electrochemical measurements are recorded using a Vertex.5Apotentiostat/galvanostat instrument by Ivium Technologies. The measurements were started at constant OCV. The fuel check, voltage-current curve (I-V curve) start at OCV to 0.6V back to OCV were recorded at a scan rate of 10 mV/s. Electrochemical impedance spectroscopy (EIS) data was collected at OCV with a frequency range from 110 kHz to 0.11 Hz, with an alternative current (AC) amplitude of 50 mV and 21 frequencies per decade.

The fuel check is done in order to know if the cell is a good contact with the current collector. The current value has to be around 2.5 A, if the current exceeds this value, the cell might shut down to prevent any damage or safety issues. After the fuel electrode reduction and Fuel Cell check, the device is switch from dry to wet condition to perform SOEC measurements.

Table 1: Steps followed in the introduction of gases for the reduction of NiO-YSZ to Ni-YSZ for single cell.

Step number	**H_2 ($Nl \cdot h^{-1}$)**	**N_2 ($Nl \cdot h^{-1}$)**	**Air ($Nl \cdot h^{-1}$)**
0	-	6	6
0.5	0.5	6	6.5
1	1	6	7
2	2	6	8
3	3	6	9
4	4	5	9
5	5	4	9
6	6	3	9
7	7	2	9
8	8	1	9
9	9	0	9

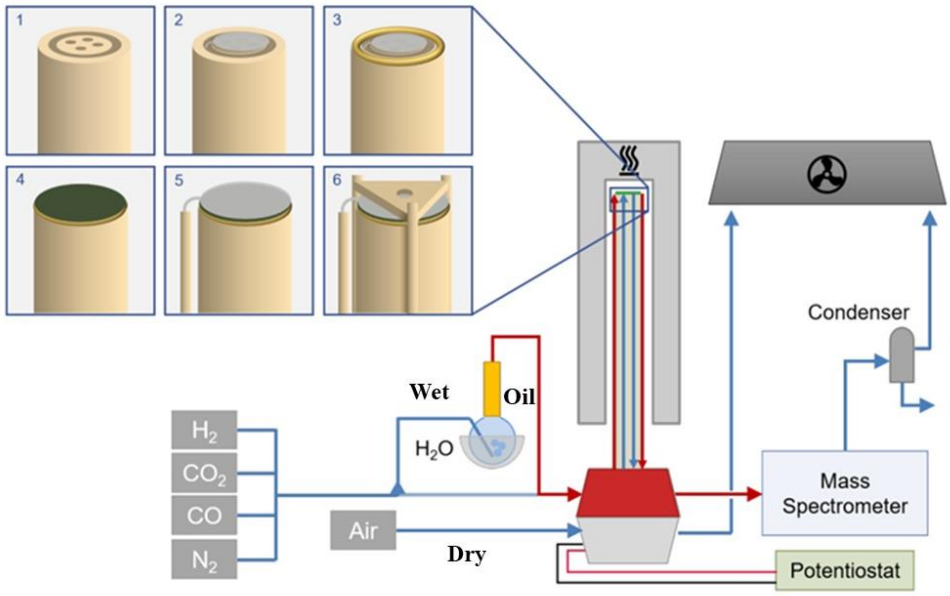

Figure 9: Schematic diagram of the experimental setup.

2.2. Electrochemical characterization

During the electrochemical characterization, different parameters were varied such as temperature of the cell and gas composition at fuel electrode. At constant OCV, I-V curves from OCV to 0.6 V to 1.4 V back to OCV were recorded at a scan rate of 10 $mV \cdot s^{-1}$and EIS data was collected with a frequency range from 110 kHz to 0.11 Hz, with an AC amplitude of 50 mV and 21 frequencies per decade. The impedance measurements were also captured in steps of 50mV from 0.7 V to 1.3 V. The frequency range used for the measurement spanned from 110 kHz to 0.11 Hz, with an AC amplitude of 0.05 V and 21 frequencies per decade. The I-V curve data was analyzed using Origin software and The EIS data was evaluated using Origin software and analyzed using DRT and ECM with the Relaxis® software.

2.2.1. Variation of Temperature

To switch from dry to wet condition, the water bath was heated at 140°C in order to get bath temperature around 93°C. Oil bath is added at a temperature of 86°C to regulate the steam vapor pressure and Hydrogen gas was used as carrier gas to transport the steam to the cell. The water bath was heated to an elevated moisture level of 60% pH_2O and utilizing 3.6 $Nl \cdot h^{-1}H_2$ as the

remaining 40 %. To avoid condensation of steam in the pipe, the gas line leading to the input of the cell is thermally insulated and heated to 170 °C. At the oxygen electrode, 9Nl·h^{-1} air was used. The voltage-current and the impedance spectroscopy measurements were recorded at different temperatures of the cell from 900 °C to 700 °C with steps of 25 °C. Voltage-current curves from OCV to 0.6 V to 1.4 V back to OCV were recorded at a scan rate of 10 mV·s^{-1}. The impedance measurements were captured in steps of 50mV from 0.7 V to 1.3 V with the frequency range from 110 kHz to 0.11 Hz, an AC amplitude of 0.05 V and 21 frequencies per decade.

2.2.2. Variation of Steam Content

On a different cell the content of steam was controlled by adjusting the water bath temperature. Different oil bath temperatures were used to adjust the steam concentration based on the temperature dependence of the vapor pressure using a Humidity calculator software to calculate the percentage of the steam. At the various oil bath temperatures of 86 °C, 82 °C, 77 °C, 70 °C, 62 °C, and 51 °C, the corresponding seawater steam concentrations were 60 %, 50 %, 40 %, 30 %, 20 %and 10 %. The temperature of the cell was set to 800 °C. At each composition, I-V curves was measured as described before and impedance spectra was recorded at OCV with a frequency range from 110 kHz to 0.11 Hz, with an AC current amplitude of 50 mV and 21 frequencies per decade.

2.2.3. Short-term Degradation

First, the short-term degradation test was conducted at different contents of steam (60 %, 50 % and 40 %) with H_2 as balance at the fuel electrode at 800 °C and 1.25Vfor 10 hours with 9 Nl·h^{-1} of air supplied to the oxygen electrode and the corresponding seawater steam /hydrogen ratios were 1.5, 1 and 0.66 at the fuel electrode.

The cell's electrochemical performance was evaluated at 800 °C before and after the extended durability test. To assess the performance, the I-V curve and EIS measurements were conducted. The EIS was recorded at OCV with 21 points/decade in a frequency range from 110 kHz to 0.11Hz with AC an amplitude of 0.05 V. I-V curves from OCV to 0.6 V to 1.4 V to OCV were recorded at a scan rate of 10 mV·s^{-1}.

Second, the short-term degradation test was conducted at different temperatures of the cell (750°C, 800°C and 850°C) at 1.25 V for 48 hours with 9 Nl·h^{-1} of air supplied to the oxygen

electrode and 40 % H_2 + 60 %H_2O to the fuel electrode. The I-V curve and EIS measurements at OCV (at the same frequency range and amplitude) were conducted.

Conclusion

In conclusion, this chapter outlines the comprehensive materials and methods used in our study to investigate the performance and durability of SOECs, particularly in seawater electrolysis for hydrogen production. The next chapter will present and discuss the results obtained from these experiments, shedding light on the behavior of the single button cell under various conditions and offering insights into potential applications for clean energy production.

CHAPTER III: RESULTS AND DISCUSSIONS

CHAPTER III: RESULTS AND DISCUSSIONS

Introduction

To investigate the effect of seawater on the performance of SOEC, different parameters were studied such as temperature, steam content and short-term stability.

1. Current-Voltage curves

Electrochemical measurements of the cell were performed after the reduction of the fuel electrode. The current-voltage characteristics were obtained at various cell temperatures between 700 °C to 900 °C, as well as the variation of steam content at 800 °C. The comparison of seawater and pure water at 800°C was also investigated.

1.1. Comparison between seawater and pure water at 800 °C

Figure 10 shows the I-V curves of pure water and seawater electrolysis at 800 °C with a gas composition of 60 % H_2O and 40 % H_2 (measured on two separate cells). A slight shift between pure water and seawater is observed. The current densities reached in electrolysis operation at 1.4 V for the utilization of pure water and seawater are -2.311 $A \cdot cm^{-2}$ and -2.14 $A.cm^{-2}$, respectively. The ASR values calculated at -0.1 $A \cdot cm^{-2}$ are 0.16 $\Omega \cdot cm^2$ and 0.030 $\Omega \cdot cm^2$ for pure water and seawater, respectively, and their OCV are 0.923 V for seawater and 0.925 V for pure water, respectively. The difference in OCV can be considered negligible. However, the current density at 0.6 V during an initial fuel cell operation check with 100 % H_2 at 900 °C can be considered negligible as well (3.55 $A \cdot cm^{-2}$ for pure water and 3.59 $A \cdot cm^{-2}$for seawater). However, the performance of sea water is similar to the performance of pure. Further experiments have to be conducted such as detailed EIS measurements and analysis to get more insight.

Lim et al. [7] studied the comparison between pure water and synthetic seawater (NaCl, $MgCl_2$ and other salts added to a pure water in specific concentration) at 800 °C with a gas composition of 70 % H_2O and 30 % H_2. After all the investigation, the result shows no influence of seawater on the cell performance and no salt was transported to the cell operated with the synthetic seawater. Similar ASR values were obtained for both the synthetic seawater (0.24 $\Omega \cdot cm^2$) and the pure water (0.23 $\Omega \cdot cm^2$ at -1 $A \cdot cm^{-2)}$. This result is in agreement with the observation shown in **Figure 10**, that the I-V curves for seawater and pure water are similar**.**

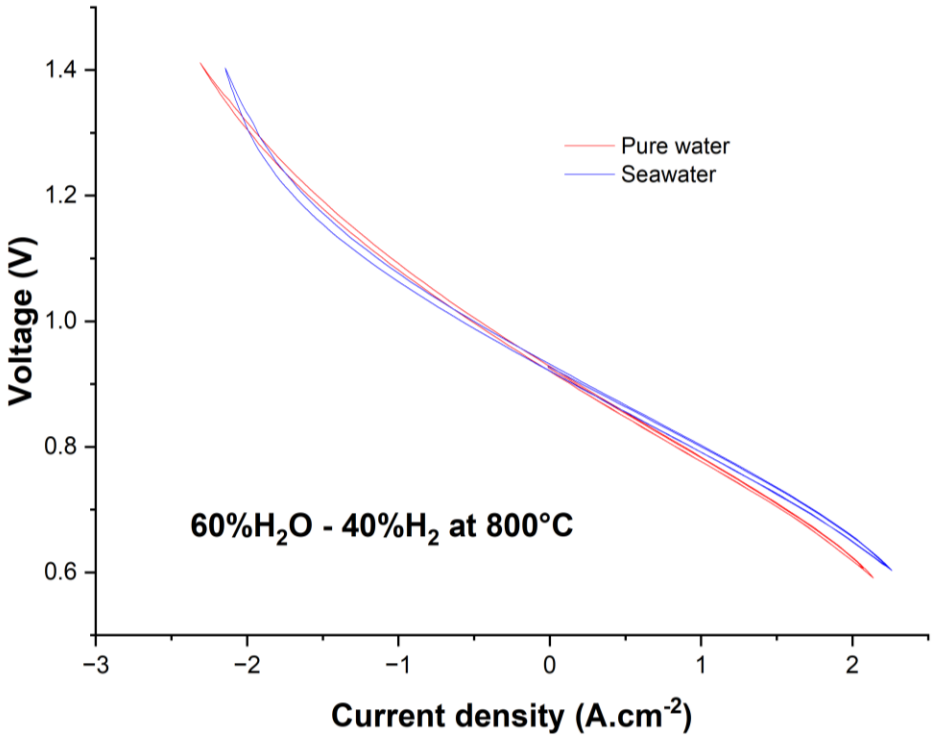

Figure 10: I-V curves of pure water and seawater at 800 ℃ with a gas composition of 60 % H_2O and 40 % H_2 measured on two distinct cells.

1.2. Temperature dependency

Figure 11 shows the electrolysis performance of the cell at different temperatures in the range of 700 ℃ to 900 ℃ with 25 ℃ steps. At low current density, the I-V curve is linear. This region is limited by ohmic resistance. As the current density is further increased, the I-V curve starts ceases to be linear for the high operating temperatures of 800 ℃ to 900 ℃, which might be due to the limitation by mass transfer. At low temperatures from 700 ℃ to 775 ℃ the mass transfer limitation seems to be not as pronounced.

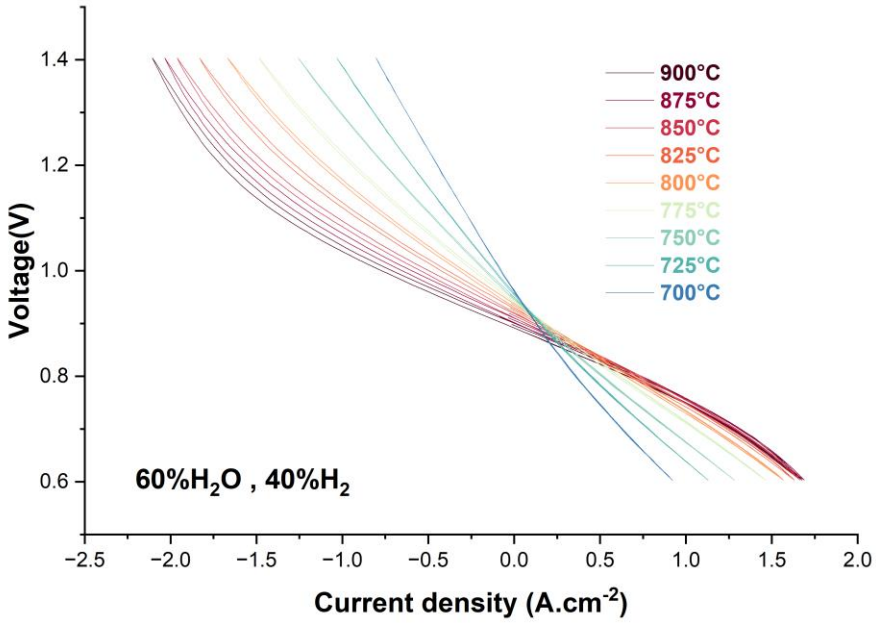

Figure 11:I-V curves of SOEC (negative current densities) and SOFC (positive current densities) of the electrolysis cell at different temperatures from 900 ℃ to 700 ℃ with 25 ℃ steps for a gas composition of 60 % H_2O and 40 % H_2.

Table 2 shows the values calculated from the graphs. The SOEC mode occurred at negative currents while the SOFC mode at positive currents. The current density at 1.4 V increases from -0.803A·cm^{-2} at 700 ℃ to -2.106 A·cm^{-2} at 900 ℃. In fuel cell mode at 0.6 V, there is an exponential increase of current density with increasing temperature from 0.923 A·cm^{-2} at 700 ℃ to 1.677 A·cm^{-2} at 900℃. The experimental OCV value decreases with increasing temperature, starting from 0.964 V at 700 ℃ to 0.897 V at 900 ℃, and the experimentally determined OCV closely aligns with calculated values from the Nernst equation. The deviation range is between 11 mV and 7 mV, and the biggest value of the deviation is attributed to the temperature of 775 ℃.

Furthermore, an exponential increase of the ASR was observed with decreasing temperature, starting from 0.150 Ω·cm^2 at 900 ℃ and reaching its highest value of 0.510 Ω·cm^2 at 700 ℃. The decrease can be generally explained by a decreased ionic conductivity and reduced kinetics. However, the specific processes that are involved cannot be determined from the IV curve alone and have to be analyzed by EIS (see Section 2).

Table 2: Theoretical and experimental OCV, $j_{0.4V}$, $j_{0.6V}$ and ASR at -0.1A·cm^{-2} for a gas composition of 60 % H_2O + 40 % H_2 at temperature from 700 °C to 900 °C with 25 °C steps, obtained from the I-V curves of Figure 11

Temperature (°C)	**$OCV_{theo.}$ (V)**	**$OCV_{exp.}$ (V)**	**$J_{1.4V}$ (A·cm^{-2})**	**$j_{0.6V}$ (A·cm^{-2})**	**ASR $_{-0.1A\cdot cm^{-2}}$ (Ω·cm^2)**
700	0.956	0.964	-0.803	0.923	0.510
725	0.948	0.957	-1.032	1.130	0.440
750	0.941	0.949	-1.256	1.282	0.360
775	0.933	0.944	-1.482	1.464	0.310
800	0.925	0.935	-1.668	1.576	0.300
825	0.917	0.926	-1.831	1.632	0.230
850	0.908	0.915	-1.961	1.665	0.220
875	0.899	0.906	-2.034	1.688	0.170
900	0.890	0.897	-2.106	1.677	0.150

1.3. Steam content dependency

Figure 12 shows the I-V curves of the solid oxide cell under different contents of steam produced from seawater at 800 °C with H_2 as balance gas. At low current density, parallel and linear curves are observed, probably caused by similar ohmic resistances. The steam flux to the TPB is fast enough so that no mass transport limitations occur in that range. At high current density, the influence of steam on the current density becomes more pronounced, the diffusion also becomes significant, and the flux is not sufficient, which increases the potential. High steam concentrations might change the concentration gradient and result in increased flux. Thus, an increased current density can be obtained. At fuel cell mode, the slope is still constant from 3 A·cm^{-2} to 0 A·cm^{-2}, a straight line is observed.

The obtained values are given in **Table 3.** When the system is operated at 1.4 V, and the steam content is increased, the current density increases from -0.629 A·cm^{-2} for 10 % H_2O (23% of steam utilization) to -2.146A·cm^{-2} for 60 % H_2O (13% of steam utilization). In fuel cell mode at 0.6 V,

there is an exponential increase of current density with an increase of steam concentration from 2.936 $A \cdot cm^{-2}$ at 10 % to 2.198 $A \cdot cm^{-2}$ at 60 %.

The experimental values of OCV decrease with increasing steam content, starting from 1.020 V at 10 % H_2O to 0.916 V at 60 %H_2O. The experimental OCV is lower than the theoretical OCV and the difference between OCV_{exp} and OCV_{theo} is not the same for all steam concentrations. The deviation is between 25 mV and 9 mV and this could be due to slight deviations in the partial pressure of the fuel gas as the steam concentration is varied.

Furthermore, an exponential increase of the ASR was observed with decreasing steam concentration, starting from 0.03 $\Omega \cdot cm^2$ at 60% and reaching its highest value 0.270 $\Omega \cdot cm^2$ at 10%. It is difficult to determine the exact process causing the ASR decrease because the value of ASR is the total resistance value at each temperature. Therefore, the cell is also characterized by EIS (see Section 2).

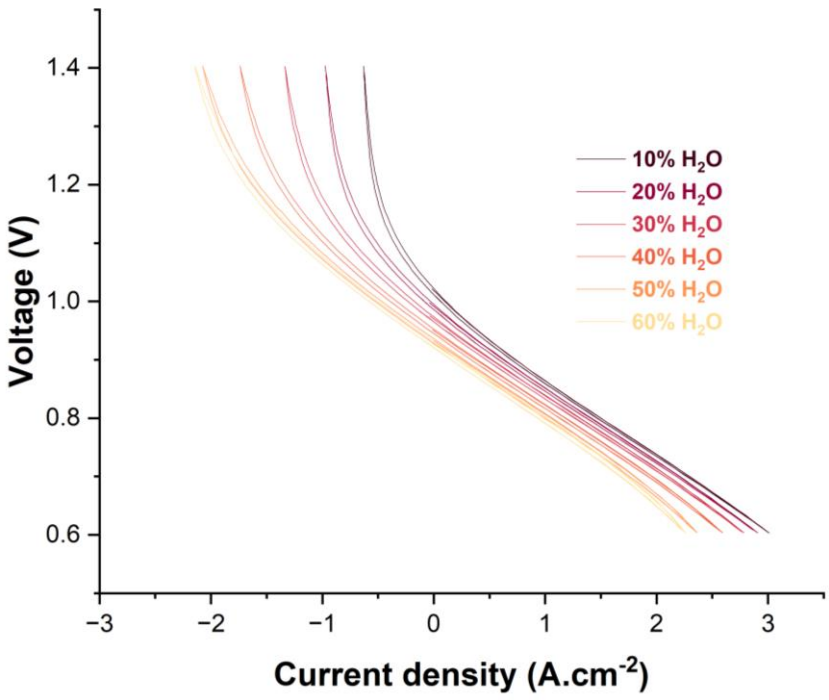

Figure 12:I-V curves of SOEC and SOFC of the cell at steam variation of 10 % to 60 % H_2O balanced with H_2 at 800 °C.

Table 3: Theoretical and experimental OCV, $j_{0.4V}$, $j_{0.6V}$ and ASR at -0.1A·cm^{-2} for steam variation at temperature 800 °C, obtained from the I-V curves of **Figure 12**.

Steam content (%)	**$OCV_{theo.}$ (V)**	**$OCV_{exp.}$ (V)**	**$j_{1.4V}$ (A·cm^{-2})**	**$j_{0.6V}$ (A·cm^{-2})**	**$ASR_{-0.1A.cm-2}$ (Ω·cm^2)**
10	1.045	1.020	-0.629	2.936	0.270
20	1.008	0.991	-0.973	2.870	0.180
30	0.983	0.969	-1.336	2.766	0.160
40	0.962	0.948	-1.739	2.542	0.150
50	0.944	0.932	-2.075	2.321	0.090
60	0.925	0.916	-2.145	2.198	0.030

2. Electrochemical impedance spectroscopy

2.1. Temperature dependency

2.1.1. Measurement at OCV

Figure 13 shows the impedance spectra at OCV at different temperatures from 700 °C to 900 °C with steps of 25 °C for a gas composition of 40 % H_2 and 60 % H_2O. Two semi-circles are observed at temperatures of 700 °C, 725 °C and 750 °C. An increase in the operating temperature leads to a shift of the spectra towards lower resistance. The dependence of temperature is seen for both ohmic resistance (R_Ω) and polarization resistance (R_p). The literature has shown that this shift towards smaller resistance is attributed to the enhanced ionic conductivity of YSZ, GDC and LSC, coupled with the improved electronic conductivity of LSC. Also, the increase in temperature leads to an increase in the reaction kinetics of the electrode leading to a shift towards lower resistances [37].

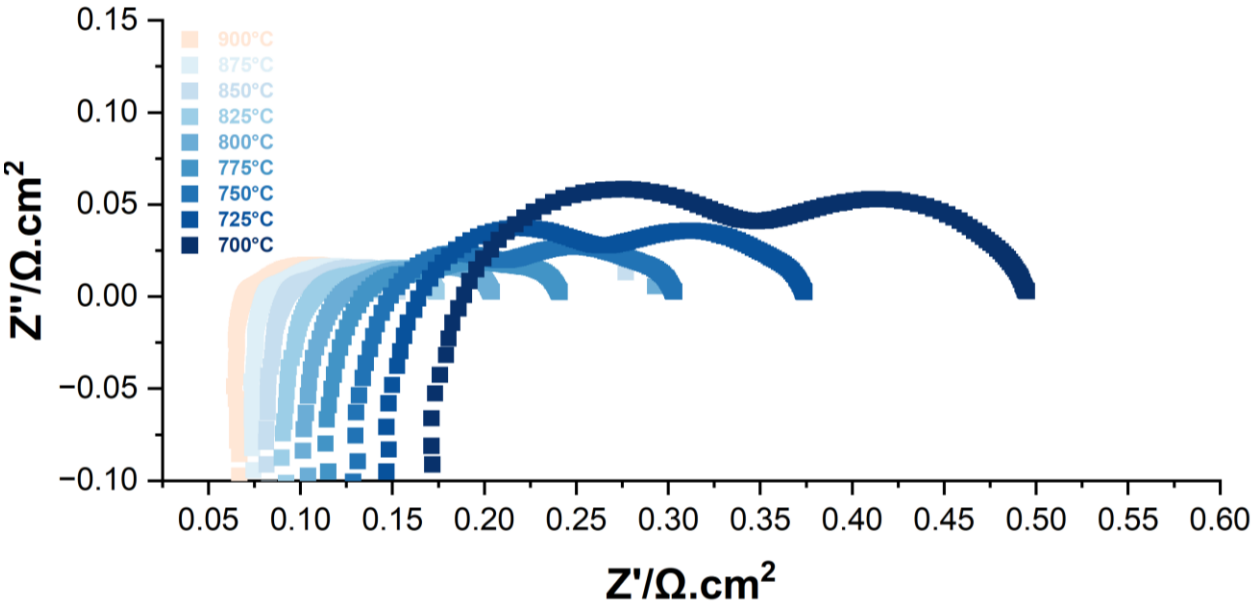

Figure 13: Nyquist plot of the electrolysis cell at temperature range from 700 ℃ to 900 ℃ with 25 ℃ steps for a gas composition of 60 % H_2O and 40 % H_2.

Nevertheless, the potential presence of overlapping time constants makes it challenging to differentiate distinct processes solely from the Nyquist plots. As a result, a deeper investigation of the impedance spectra is conducted using distribution of relaxation time (DRT) analysis, as depicted in **Figure 14.**

DRT is used to deconvolute various processes in the frequency domain that collectively influence the overall impedance response of the cells. The investigation on how DRT peaks are affected by changes in temperature, different temperatures from 700 ℃ to 900 ℃ with 25 ℃ steps were utilized. In **Figure 14**, four peaks were observed (P_1-P_4). P_1, P_2 and P_3 showed an increase in magnitude with a decrease in temperature, with the P1 peak exhibiting the highest increase in magnitude. Also, P_2 and P_3 peaks shifted to lower frequencies with the decrease in temperature from 900℃ to 775℃. The impact of temperature is not significant for the peak P_4.

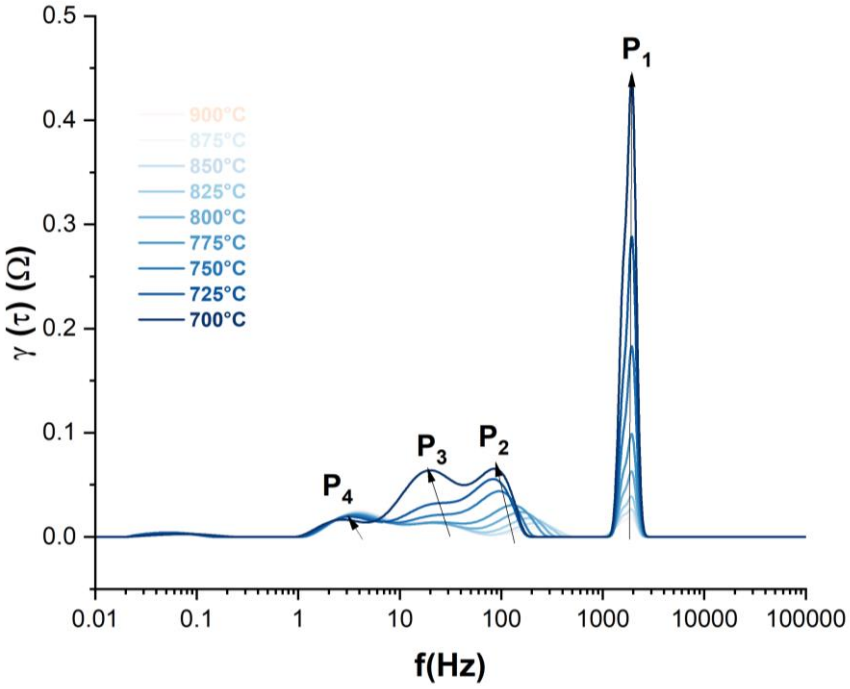

Figure 14:DRT plot of the electrolysis cell at OCV at different temperature from 900 ℃ to 700 ℃ with 25 ℃ steps with a gas composition of 60 % H_2O and 40 % H_2, obtained from the EIS spectra of Figure 13.

The analysis of the EIS with an ECM offers a comprehensive representation of the processes taking place in the cell during steam electrolysis. This ECM comprises an inductance element *I* connected in series with an ohmic resistor (R_Ω), alongside the inclusion of four Resistor-Constant Phase Element (4RQ) components. The ohmic resistor is responsible for accounting for the losses attributed to ohmic resistance. Four RQ elements, as demonstrated in **Figure 15**, were utilized because four different peaks (time constants) were observed in the DRT plot.

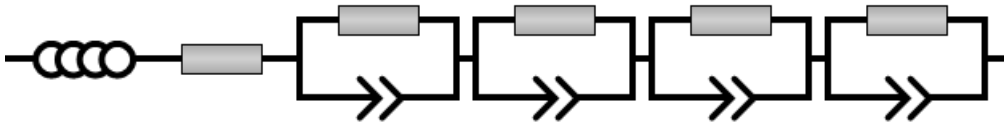

Figure 15:ECM containing an inductance in series with a serial resistor and 4 RQ-elements used to fit the impedance spectra.

Figure 16 shows the Nyquist plot for a gas composition of 60 % H_2O and 40 % H_2at 850 ℃ and the respective fit of the individual time constant. While **Figure 17** shows the residuals

(difference of data and fit) of the real and imaginary part of the spectrum shown in **Figure 16**. It shows a sinusoidal shape, which indicates that the model is not perfectly fitting. Thus, the model needs to be improved in future analyses. For the scope of this thesis, the model describes the data reasonably well.

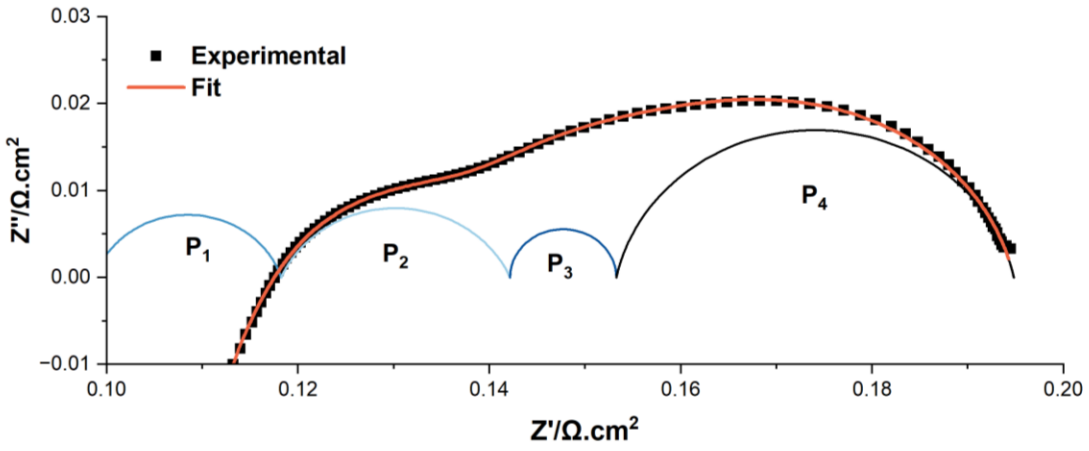

Figure 16: Nyquist plot of the gas composition of 60 % H_2O and 40 % H_2at 850°C and the respective fit of the individual time constants.

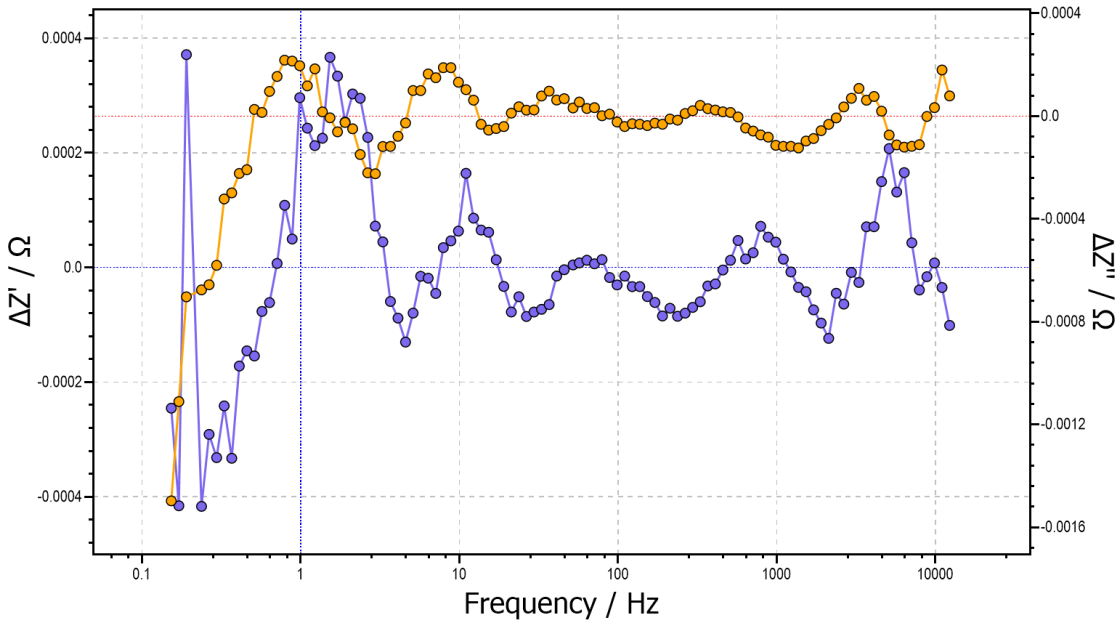

Figure 17: Residuals (difference of fit and data) of the fit shown in Figure 16.

The obtained resistance values from the ECM fit are used to calculate the activation energy E_A (kJ/mol) according to the Arrhenius equation (equation 17) by plotting ln (R) versus 1/T (Figure 18). From the slope and the universal gas constant R_g of the linear fit, the activation energy is calculated.

$$\boldsymbol{lnR = -\ln \sigma_{\circ} + \frac{E_A}{R_g T}} \qquad \textbf{(17)}$$

Figure 18 illustrates the Arrhenius plot of the resistances at OCV conditions. The graph shows that the resistances R_{RQ1}, R_{RQ2} andR_{RQ3}, decrease with an increase in temperature. This implies that the underlying electrochemical processes are thermally activated. However, R_{RQ4} shows a contrary trend. It rather increased with increasing temperature. The reason for this behavior is still uncertain, however further analysis will provide more insight. **Table 4** illustrates the obtained activation energies for the resistances. R_{RQ1}, R_{RQ2} and R_{RQ3} all show very high activation energy meanwhile R_{RQ4} shows a negative activation energy.

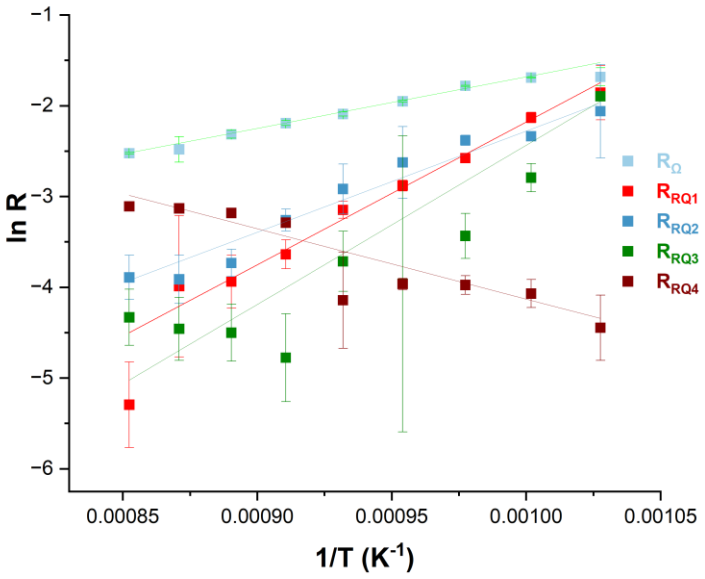

Figure 18: Arrhenius plot of the ohmic resistance Rω and resistance of RQ-elements in steam electrolysis during variation of temperature from 700 °C to 900 °C with 25 °C steps with a gas composition of 60 % H_2O and 40 % H_2.

Table 4: Values of activation energies for R_Ω and R_{RQ1}, R_{RQ2}, R_{RQ3} and R_{RQ4} obtained from the slope of a linear fit of the Arrhenius plot in Figure 18.

Parameters	$E_{A,\,OCV}$ (kJ · mol^{-1})
R_Ω	47 ± 1
R_{RQ1}	130 ± 7
R_{RQ2}	92 ±9
R_{RQ3}	145 ±16
R_{RQ4}	-64 ±9

2.1.2. Measurement under polarization

To further evaluate the electrode processes, impedance data was also obtained under polarization. **Figure 19** shows the Nyquist plot of the impedance spectra for the seawater of EC and FC mode at 900 °C for a gas composition of 60 % H_2O and 40 % H_2 as a function of polarization. The Nyquist plot shows the presence of two characteristic arcs: a high frequency and a low frequency arc. The low frequency arc shows a more pronounced dependence on the increase in polarization from OCV (0.897 V) to 1.3 V while the high frequency arc illustrates a slight change with an increase in the operating voltage. Overall, the Nyquist plot shows that the Rp increases with an increase in polarization from OCV to 1.3 V. From 0.7V to OCV, the low and high frequency doesn't show a significant change in term of variation of polarization, The change of ohmic resistance is also observed.

Figure 20 shows the DRT plot of the impedance spectra as a function of polarization. From the plot, all the peaks exhibited significant dependence on the polarization variation. However, P_4 illustrates the most pronounced dependence on polarization. Under polarization steam has been consumed. This means that the ratio of hydrogen to steam in the fuel gas is influenced by the polarization. Therefore, P_4 strongly depends on this changing ratio. The underlying P_4 process strongly depends on this changing ratio, which suggests a gas diffusion in the fuel electrode. The peak between the range 0.1Hz- 1Hz is outside of the measurement range, this peak can be assigned to the noise during the electrochemical measurement.

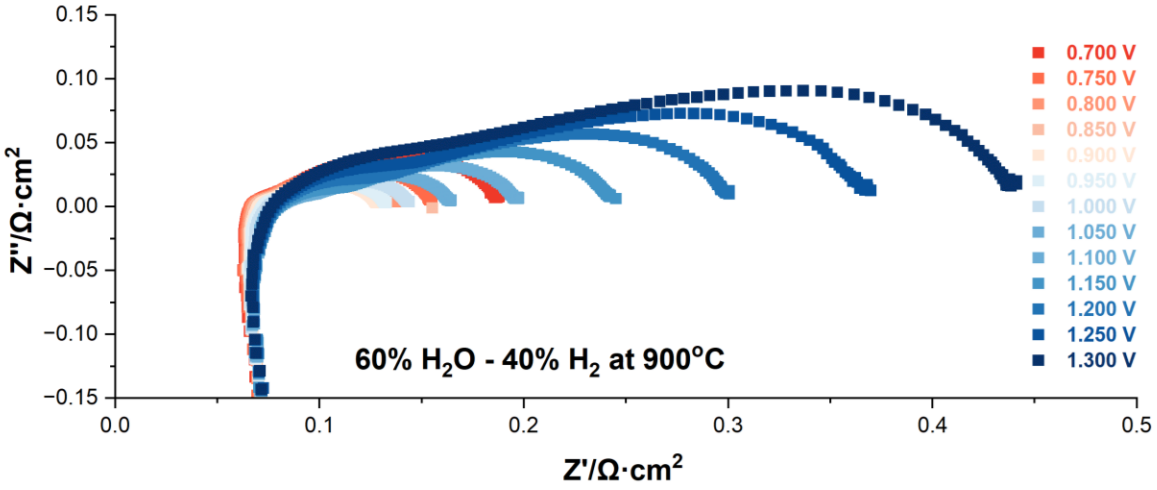

Figure 19: Nyquist plot of the electrolysis cell under polarization from 0.7 V to 1.3 V at 900 °C with a gas composition of 60 % H_2O and 40 % H_2.

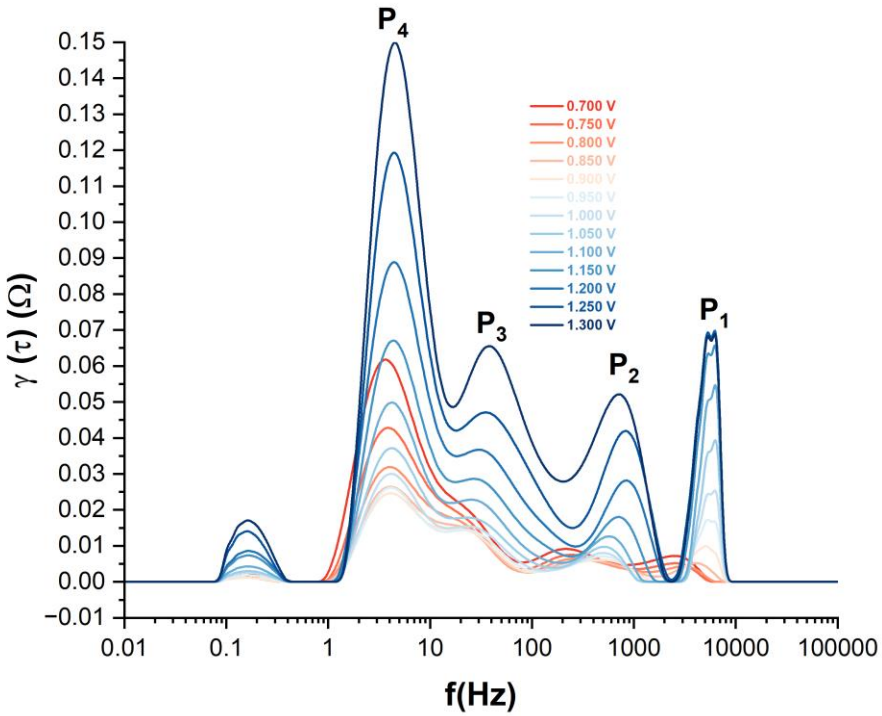

Figure 20:DRT plot of the electrolysis cell under polarization from 0.7 V to 1.3 V at 900 °C obtained from the spectra shown in Figure 19.

2.2. Steam content dependency

Impedance spectra were also obtained as a function of steam content variation to identify the electrochemical processes originating from the fuel electrode. **Figure 21** illustrates the Nyquist plot of steam concentration variation at 800 ℃. The decrease in H_2O content leads to an increase in the Rp of the Nyquist plot, especially for the low frequency regime, where the semicircle increases in magnitude in both the real and imaginary parts. A slight change is also visible in the high frequency regime. The Rω also shows a slight increase with the variation of steam concentration.

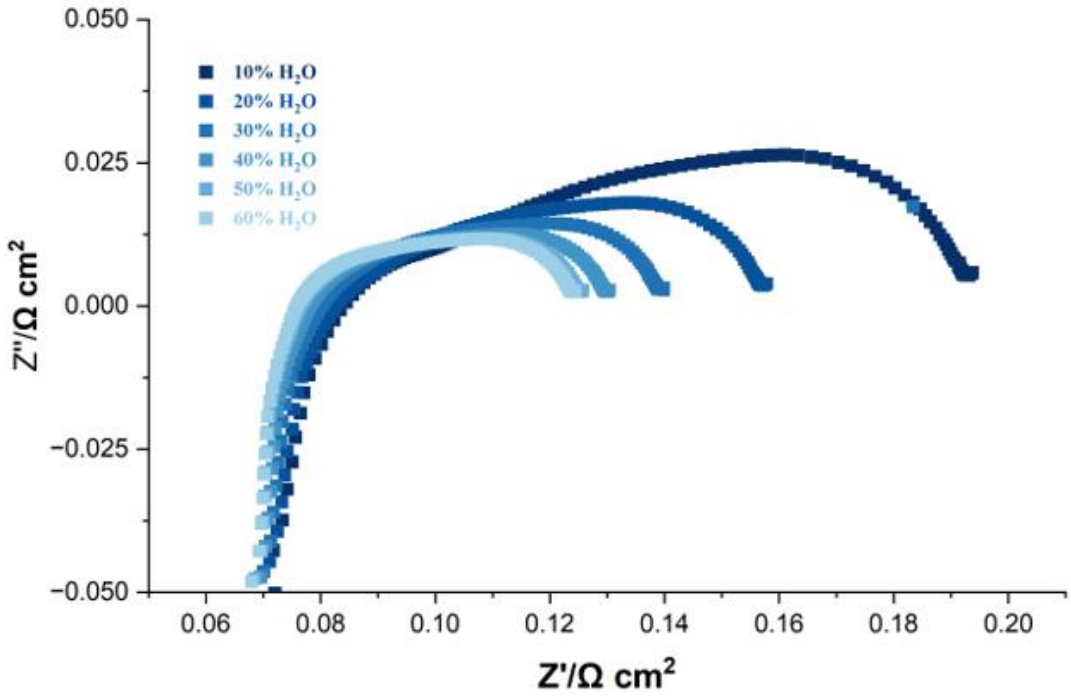

Figure 21: Nyquist plot of the electrolysis cell at different steam variations at 800 ℃.

Figure 22 illustrates the corresponding DRT plot as a function of steam content variation at OCV. From the plot, all the peaks (P_1 –P_4) show observable dependency to steam partial pressure variation, increasing in magnitude with decrease in steam content. P_4 and P_1 exhibited the most pronounced dependency on steam variation.

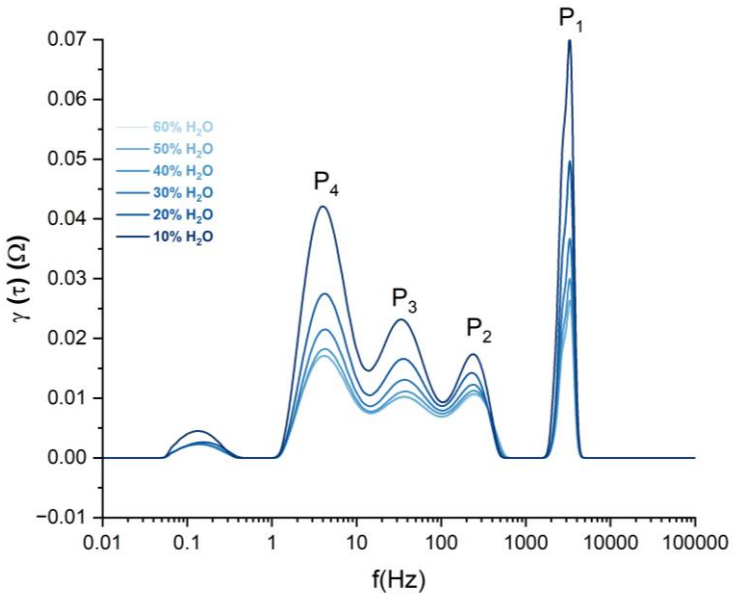

Figure 22: DRT plot of the electrolysis cell at different steam variations at 800℃

The double logarithmic plot of the variation of steam concentration at 800 ℃ is shown in **Figure 23**, and the plot matches with the DRT plot. $R_{RQ1,}$ R_{RQ2} andR_{RQ3} decreased with an increase in the steam concentration. This confirms that there is dependency of steam concentration. The Rω and R_{RQ4} are almost constant with the variation of steam.

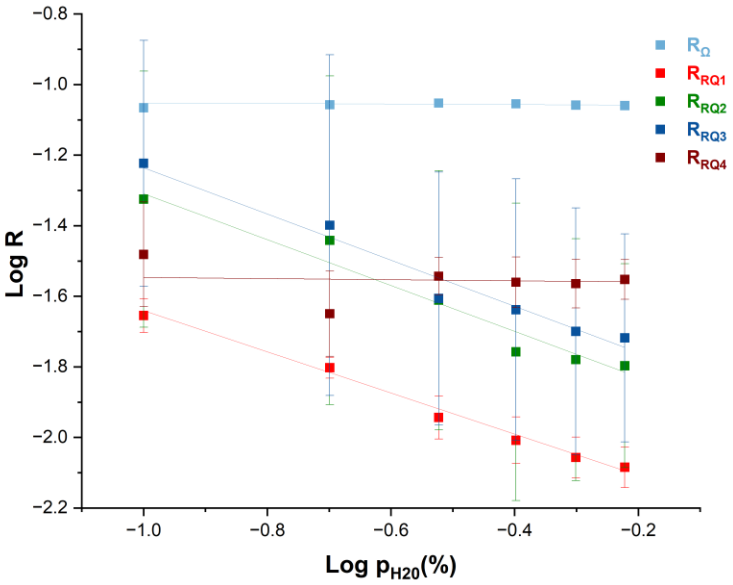

Figure 23: Double logarithmic plot of the ohmic resistance Rω and resistances of RQ-elements in steam electrolysis during variation of steam concentration at 800 ℃.

❖ **Assignment of electrochemical processes.**

From the DRT and ECM fitting, four electrochemical processes are identified; P_1, P_2, P_3 and P_4 representing $R_{RQ1,}$ $R_{RQ2,}$ R_{RQ3} and R_{RQ4}. The peak P_1 shows high activation energy of 131 $kJ \cdot mol^{-1}$ (1.35 eV) and it is located in the high frequency regime. In literature, Caliandro et al. [37] assigned this process to the charge transfer at the fuel electrode according to the range of frequency (0.5-up to 100 kHz).

The mid frequency processes of P_2 and P_3 also exhibited significant temperature dependency. This indicates that the underlying electrochemical processes are thermally activated processes. The relaxation frequency of these processes as well as the high activation energy is similar to those reported in [38,39] for transport processes at both the oxygen electrode and fuel electrode. These transport processes in the LSCF electrode include oxide ion transport and surface exchange kinetics. Therefore, considering that the intermediate frequencies of P_2 and P_3 also show significant steam content variation, it is possible that these processes are transport processes at both the fuel and oxygen electrode.

With regards to the low frequency process of P_4, the peak shows significant steam content dependency indicating that it is a fuel electrode process. Also, the relaxation frequency of this process is common for a diffusion process in the fuel electrode [40].However, diffusion processes do not show negative activation energies. Hence, it is possible that this process is a diffusion process in conjunction with other electrochemical processes.

Overall, further analysis such as impedance under variation of partial pressure of oxygen is needed to validate these assigned processes.

3. Short-term degradation

3.1. Steam content dependency

The time-plot of the current density at an applied potential of 1.250 V for 10 hours at different steam concentrations is shown in Figure 25. The according values from the curves can be seen in **Table 5**. Decreasing the partial pressure of the steam will decrease the current density from 1.282 $A \cdot cm^{-2}$ at 60 % to 1.041 $A \cdot cm^{-2}$ at 40 %. And this can be confirmed in previously discussed I-V curve (**Figure 12**). After degradation a decrease of current density is observed with

a degradation rate between 2.6 mA·cm^{-2}/hand 0.3 mA·cm^{-2}/h for 50 % and 60 % steam, respectively. The high degradation rate is attributed to the steam concentration of 50%.

Singh et al. [41] investigated the short-term degradation at constant voltage (1.286 V) at different steam concentrations (74 %, 71 %, 67 %, 62 % and 54 %) for 10 hours. They concluded that the corresponding electrolysis current density at thermal neutral voltage decreases as the partial steam pressure decreases, leading to a lower degradation rate of the cell.

They also state that at water bath temperature of 86 °C (54 % of the steam content), a noticeable rise in the degradation rate occurs, indicating a shift in the primary reaction mechanism. This intriguing occurrence can be attributed to the occurrence of steam starvation under these temperature conditions. When the water bath temperature reaches 86 °C, the cell experiences elevated concentration polarization even when operating at a thermally neutral voltage. This heightened concentration polarization could potentially contribute to more pronounced degradation during prolonged periods of operation [41].

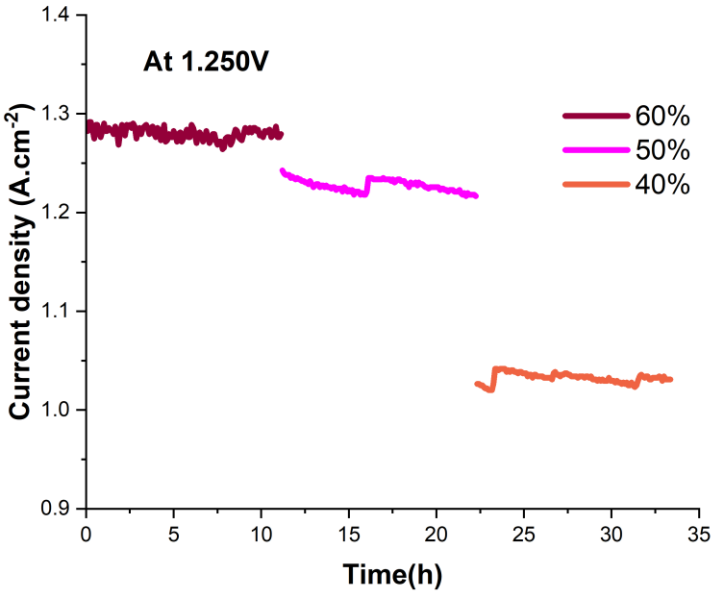

Figure 24:I-t curve of short-term degradation at 1.250 V for 10 h of electrolysis cell under steam variation.

Table 5: Variation of the current density of seawater electrolysis and the degradation rate of the cell under different water bath temperatures and thermal neutral voltage

steam content (%)	Initial current density ($A \cdot cm^{-2}$)	Final current density ($A \cdot cm^{-2}$)	Degradation rate ($mA \cdot cm^{-2}/h$)
60	1.282	1.279	0.3
50	1.242	1.216	2.6
40	1.041	1.031	1

3.2. Temperature dependency

3.2.1. Short term degradation

Figure 24 shows the I-t curve obtained from the short-term degradation measurement at different temperatures for 48 hours at a constant voltage of 1.250 V at 850 ℃. A slow decrease in current density with time is observed. There are also traces of fluctuations that can be attributed to unknown reactions during the degradation or instabilities in the system.

The second experimented temperature 800 ℃ displays a very different pattern of current density variation. A slow and fluctuation-free decrease is first observed with values of current density lower than for the temperature of 850 ℃. Then there is a sudden change in slope at around 100 hours followed by heavy fluctuations.

The test carried on at 750 ℃ starts with low values and a high rate of fluctuation. We observe a sudden increase and then a relative consistency, however, some fluctuations still remain.

The experiment cannot explain completely the phenomenon of current density degradation. It could be interesting and relevant to carry out several other experiments that will be needed to effectively assess the current degradation rate.

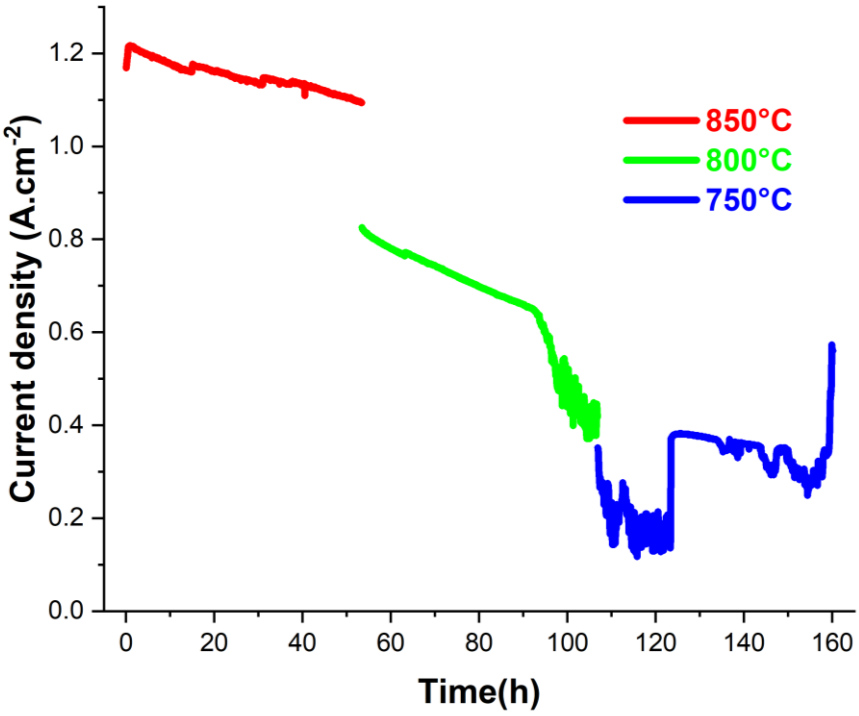

Figure 25:I-t curve of short-term degradation of electrolysis cell at 1.250V under temperature variation

3.2.2. I-V Curve before and after degradation at different temperatures

Figure 26 shows the I-V curve of short-term degradation at 850 °C. And the two curves show almost the same behavior. A slight increase of performance in EC mode after degradation is seen with an increase of current density from -1.717 $A \cdot cm^{-2}$ to -1.823 $A \cdot cm^{-2}$. An improvement in performance can be concluded. At OCV a straight-line result is observed due to the limitation of ohmic resistance. At high voltage 1.4 V and high current density a curvature is observed for both curves. This curvature can be attributed to the mass transport limitation. At low voltage 0.6 V (fuel cell mode) a decrease of performance is observed. The current density decreases after degradation. However, more experiments must be done to explain the improved performance.

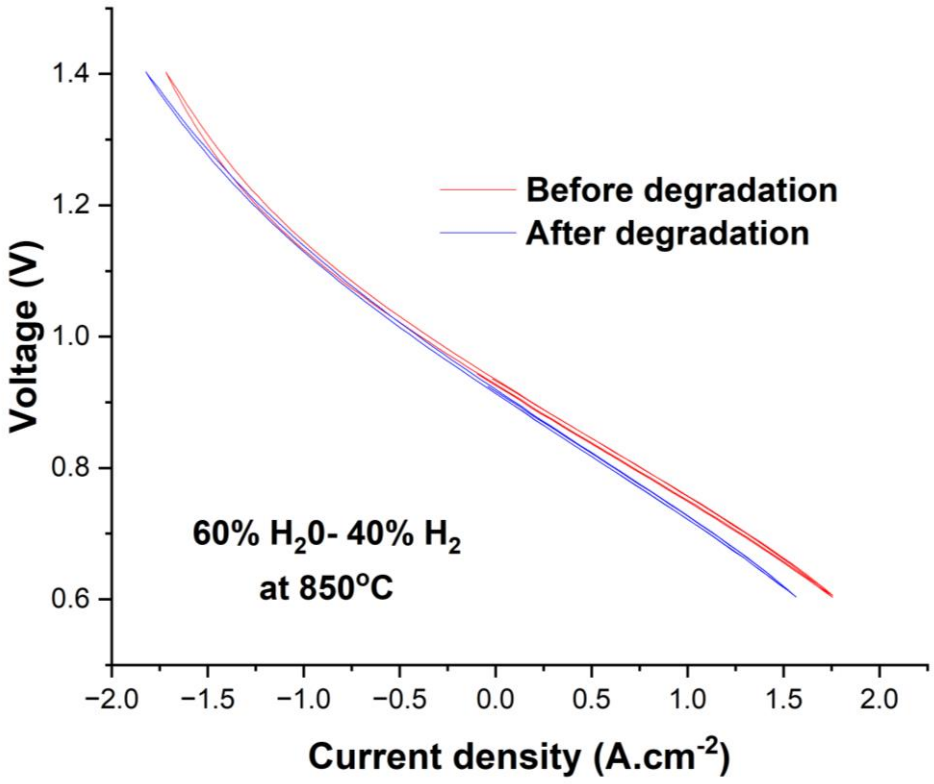

Figure 26: I-V curves of the solid oxide cell before and after the degradation at 850 °C with a gas composition of 60 % H_20 and 40 % H_2.

The I-V curves at 800 °C before and after the short-term degradation are shown in **Figure 27.** The shift is observed between the two curves showing a decrease in current density after the degradation. The degradation rate is about 0.006A·cm^{-2}/h. It is clearly shown that the performance decreases after degradation. After degradation the curve shows a different form, which may be explained by an error during the measurement. This unknown form is also observed in **Figure 28** showing the I-V curves at 750 °C before and after the short-term degradation. **Figure 28** shows a decrease of performance from -0.750 A·cm^{-2} to -0.662A·cm^{-2}. More experiments are required to understand the phenomena that appeared during the degradation.

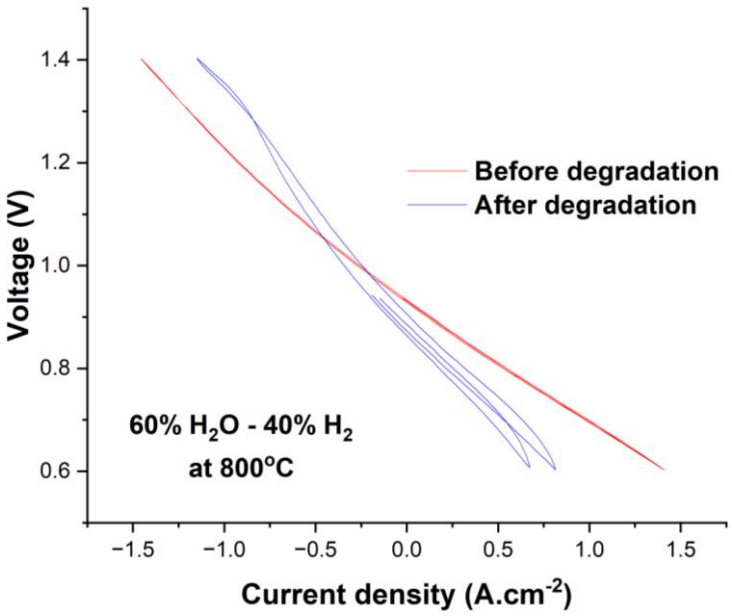

Figure 27:I-V curves of the electrolysis cell before and after the degradation at 800 °C with a gas composition of 60 % H_20 and 40 % H_2.

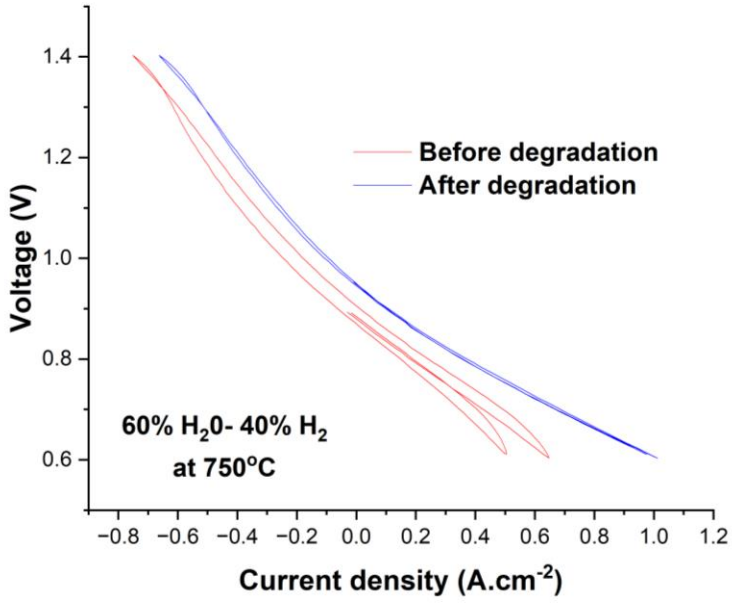

Figure 28:I-V curves of the electrolysis cell before and after the degradation at 750 °C with a gas composition of 60 % H_20 and 40 % H_2.

Conclusion

This chapter presents a comprehensive investigation into the performance of SOEC under various conditions, with a particular focus on the impact of seawater. Seawater demonstrated comparable performance to pure water at 800 ℃, with minor differences in current densities but negligible changes in Open Circuit Voltage (OCV). Temperature was found to significantly affect the SOEC, with increasing temperatures leading to higher current densities, though at the expense of lower OCV values. Steam content also played a crucial role, as higher steam concentrations resulted in increased current densities and lower OCV values. Electrochemical Impedance Spectroscopy (EIS) unveiled the temperature-dependent behavior of ohmic and polarization resistances, and DRT analysis identified distinct electrochemical processes contributing to impedance. Short-term degradation experiments demonstrated the influence of both temperature and steam content on degradation rates, with lower steam content and higher temperatures accelerating degradation. Surprisingly, in some cases, SOECs exhibited improved performance post-degradation, requiring further investigation. These findings offer valuable insights for optimizing SOEC systems in practical applications, with temperature and steam content control being critical considerations.

CONCLUSION

CONCLUSION

This study investigates the effect of seawater on SOEC. The I-V curve and EIS data were performed. During the process, three parameters were studied such as temperature, steam content variation and short-term durability.

First, the I-V curve seawater was compared to the pure water, and the performance of pure water is similar to the performance of seawater.

Second, the increase of temperature causes an increase in performance. Likewise, the increase in steam concentration shows an increase in performance. The impedance spectra show a decrease in resistance by increasing the temperature of the cell and the steam content. A comprehensive exploration of the sensitivity of the positions and magnitudes of DRT peaks concerning operational parameters has been provided.

Variation in temperature has shown that the mid frequency processes of P_2 and P_3 exhibited significant temperature dependency. This indicates that the underlying electrochemical processes are thermally activated processes. In literature this process is assigned to transport processes at both the oxygen electrode and fuel electrode. Hence, given the noticeable variation in steam content within the intermediate frequencies of P_2 and P_3, it suggests the likelihood of these processes being transport phenomena occurring at both the fuel and oxygen electrodes.

The prominent peak labeled as P1 exhibits a significant activation energy of 131 $kJ \cdot mol^{-1}$ (equivalent to 1.35 eV), positioned within the high frequency range.

The low-frequency phenomenon observed in P_4's behavior exhibits a notable correlation with steam content, suggesting its association with a fuel electrode process. This is further substantiated by the consistent relaxation frequency, characteristic of diffusion processes within the fuel electrode. It's worth noting that diffusion processes typically don't display negative activation energies. This implies the likelihood of a combined occurrence, possibly entailing a diffusion process alongside other electrochemical mechanisms. To ascertain these designated processes, additional investigations, such as impedance tests conducted under varying partial oxygen pressure conditions, are imperative.

Next, the cell was operated in steam electrolysis condition (40 %,50 % and 60 %) for 10 hours. The degradation rate was 1 $mA \cdot cm^{-2}/h$, 2.6 $mA \cdot cm^{-2}/h$ and 0.3 $mA \cdot cm^{-2}/h$. The short-term durability for 48 hours at different temperatures (850 °C, 800 °C and 750 °C) was also investigated. The degradation rate was between 0.006 $mA \cdot cm^{-2}/h$ and 0.002 $mA \cdot cm^{-2}/h$, and the highest degradation is shown at 800 °C.

In the recommendations section, it's important to note that the experiments were limited in scope. To enhance the depth of the findings, the long-term tests should be conducted for 1000 hours to assess the cell's degradation rate. Additionally, it would be valuable to explore the hydrogen production performance of seawater with another cell type, such as Ni- GDC//8YSZ//GDC//LSCF, and subsequently compare their effectiveness.

Furthermore, addressing material corrosion in electrolysis equipment is crucial. It may be relevant if going from purely ceramic setup to stacks, which involve steel. This can be achieved through two main approaches: firstly, considering the option of desalinating seawater before electrolysis, which may incur significant costs. Alternatively, efforts could be directed towards optimizing the materials used in electrolysis setups to better withstand the corrosive effects of seawater, thereby reducing corrosion rates. This holistic approach will contribute to a comprehensive understanding of the cell's long-term stability and efficiency under different conditions.

BIBLIOGRAPHIES

[1] G. Kaur, A. P. Kulkarni, and S. Giddey, "CO2 reduction in a solid oxide electrolysis cell with a ceramic composite cathode: Effect of load and thermal cycling," *International Journal of Hydrogen Energy*, vol. 43, no. 48, pp. 21769–21776, Nov. 2018, doi: 10.1016/j.ijhydene.2018.10.014.

[2] M. Ni, M. Leung, and D. Leung, "Technological development of hydrogen production by solid oxide electrolyzer cell (SOEC)," *International Journal of Hydrogen Energy*, vol. 33, no. 9, pp. 2337–2354, May 2008, doi: 10.1016/j.ijhydene.2008.02.048.

[3] "World Energy Outlook 2021".

[4] M. B. Mogensen *et al.*, "Reversible solid-oxide cells for clean and sustainable energy," *Clean Energy*, vol. 3, no. 3, pp. 175–201, Nov. 2019, doi: 10.1093/ce/zkz023.

[5] Z. Liu *et al.*, "Efficiency and stability of hydrogen production from seawater using solid oxide electrolysis cells," *Applied Energy*, vol. 300, p. 117439, Oct. 2021, doi: 10.1016/j.apenergy.2021.117439.

[6] M. R. Singh, C. Xiang, and N. S. Lewis, "Evaluation of flow schemes for near-neutral pH electrolytes in solar-fuel generators," *Sustainable Energy Fuels*, vol. 1, no. 3, pp. 458–466, 2017, doi: 10.1039/C7SE00062F.

[7] C. K. Lim, Q. Liu, J. Zhou, Q. Sun, and S. H. Chan, "High-temperature electrolysis of synthetic seawater using solid oxide electrolyzer cells," *Journal of Power Sources*, vol. 342, pp. 79–87, Feb. 2017, doi: 10.1016/j.jpowsour.2016.12.019.

[8] M. Reisert, A. Aphale, and P. Singh, "Solid Oxide Electrochemical Systems: Material Degradation Processes and Novel Mitigation Approaches," *Materials*, vol. 11, no. 11, p. 2169, Nov. 2018, doi: 10.3390/ma11112169.

[9] A. Brisse, J. Schefold, and M. Zahid, "High temperature water electrolysis in solid oxide cells," *International Journal of Hydrogen Energy*, vol. 33, no. 20, pp. 5375–5382, Oct. 2008, doi: 10.1016/j.ijhydene.2008.07.120.

[10] L. Dittrich, "Tailoring of the synthesis gas composition during high-temperature co-electrolysis".

[11] G. Jeanmonod, "Effects of impurities and local behavior characterization using active thermography on solid oxide electrolysis cells," p. 278, 2021.

[12] P. Moçoteguy and A. Brisse, “A review and comprehensive analysis of degradation mechanisms of solid oxide electrolysis cells,” *International Journal of Hydrogen Energy*, vol. 38, no. 36, pp. 15887–15902, Dec. 2013, doi: 10.1016/j.ijhydene.2013.09.045.

[13] Y. Zheng *et al.*, “A review of high temperature co-electrolysis of H_2O and CO_2 to produce sustainable fuels using solid oxide electrolysis cells (SOECs): advanced materials and technology,” *Chem. Soc. Rev.*, vol. 46, no. 5, pp. 1427–1463, 2017, doi: 10.1039/C6CS00403B.

[14] V. N. Nguyen and L. Blum, “Syngas and synfuels from H2O and CO2: Current status,” *Chemie-Ingenieur-Technik*, vol. 87, no. 4, pp. 354–375, 2015, doi: 10.1002/cite.201400090.

[15] M. A. Laguna-Bercero, “Recent advances in high temperature electrolysis using solid oxide fuel cells: A review,” *Journal of Power Sources*, vol. 203, pp. 4–16, 2012, doi: 10.1016/j.jpowsour.2011.12.019.

[16] N. Tenhumberg and K. Büker, “Ecological and Economic Evaluation of Hydrogen Production by Different Water Electrolysis Technologies,” *Chemie Ingenieur Technik*, vol. 92, no. 10, pp. 1586–1595, Oct. 2020, doi: 10.1002/cite.202000090.

[17] P. A. Connor *et al.*, “Tailoring SOFC Electrode Microstructures for Improved Performance,” *Adv. Energy Mater.*, vol. 8, no. 23, p. 1800120, Aug. 2018, doi: 10.1002/aenm.201800120.

[18] A. Nechache and S. Hody, “Alternative and innovative solid oxide electrolysis cell materials: A short review,” *Renewable and Sustainable Energy Reviews*, vol. 149, p. 111322, Oct. 2021, doi: 10.1016/j.rser.2021.111322.

[19] I. D. Unachukwu, V. Vibhu, I. C. Vinke, R.-A. Eichel, and L. G. J. (Bert) De Haart, “Electrochemical and degradation behaviour of single cells comprising Ni-GDC fuel electrode under high temperature steam- and co-electrolysis conditions,” *Journal of Power Sources*, vol. 556, p. 232436, Feb. 2023, doi: 10.1016/j.jpowsour.2022.232436.

[20] S. Ovtar, X. Tong, J. J. Bentzen, K. T. S. Thydén, S. B. Simonsen, and M. Chen, “Boosting the performance and durability of Ni/YSZ cathode for hydrogen production at high current densities *via* decoration with nano-sized electrocatalysts,” *Nanoscale*, vol. 11, no. 10, pp. 4394–4406, 2019, doi: 10.1039/C8NR07678B.

[21] C. Yang, A. Coffin, and F. Chen, “High temperature solid oxide electrolysis cell employing porous structured (La0.75Sr0.25)0.95MnO3 with enhanced oxygen electrode performance,”

International Journal of Hydrogen Energy, vol. 35, no. 8, pp. 3221–3226, Apr. 2010, doi: 10.1016/j.ijhydene.2010.01.056.

[22] A. Hauch *et al.*, "Recent advances in solid oxide cell technology for electrolysis," *Science*, vol. 370, no. 6513, p. eaba6118, Oct. 2020, doi: 10.1126/science.aba6118.

[23] C. M. Grgicak, R. G. Green, and J. B. Giorgi, "SOFC anodes for direct oxidation of hydrogen and methane fuels containing H2S," *Journal of Power Sources*, vol. 179, no. 1, pp. 317–328, Apr. 2008, doi: 10.1016/j.jpowsour.2007.12.082.

[24] K. Sasaki *et al.*, "H2S Poisoning of Solid Oxide Fuel Cells," *Journal of The Electrochemical Society*.

[25] G. Jeanmonod, S. Diethelm, and J. Van Herle, "Poisoning effects of chlorine on a solid oxide cell operated in co-electrolysis," *Journal of Power Sources*, vol. 506, p. 230247, Sep. 2021, doi: 10.1016/j.jpowsour.2021.230247.

[26] J. P. Trembly, R. S. Gemmen, and D. J. Bayless, "The effect of coal syngas containing HCl on the performance of solid oxide fuel cells: Investigations into the effect of operational temperature and HCl concentration," *Journal of Power Sources*, vol. 169, no. 2, pp. 347–354, Jun. 2007, doi: 10.1016/j.jpowsour.2007.03.018.

[27] S. Green, S. Science, T. Engineering, and C. Nanoscience, "Seawater Electrolysis".

[28] W. Tong *et al.*, "Electrolysis of low-grade and saline surface water," *Nat Energy*, vol. 5, no. 5, pp. 367–377, Feb. 2020, doi: 10.1038/s41560-020-0550-8.

[29] H. Jin *et al.*, "Single-Crystal Nitrogen-Rich Two-Dimensional Mo $_5$ N $_6$ Nanosheets for Efficient and Stable Seawater Splitting," *ACS Nano*, vol. 12, no. 12, pp. 12761–12769, Dec. 2018, doi: 10.1021/acsnano.8b07841.

[30] S. Gao *et al.*, "Electrocatalytic H $_2$ production from seawater over Co, N-codoped nanocarbons," *Nanoscale*, vol. 7, no. 6, pp. 2306–2316, 2015, doi: 10.1039/C4NR04924A.

[31] Y. Kuang *et al.*, "Solar-driven, highly sustained splitting of seawater into hydrogen and oxygen fuels," *Proc. Natl. Acad. Sci. U.S.A.*, vol. 116, no. 14, pp. 6624–6629, Apr. 2019, doi: 10.1073/pnas.1900556116.

[32] Y. Yan, *Degradation Study of SOC Stacks with Impedance Spectroscopy*, vol. 441. 2018.

[33] H. S. Magar, R. Y. A. Hassan, and A. Mulchandani, "Electrochemical impedance spectroscopy (Eis): Principles, construction, and biosensing applications," *Sensors*, vol. 21, no. 19, 2021, doi: 10.3390/s21196578.

[34] J. Benavente, *Electrochemical impedance spectroscopy as a tool for electrical and structural characterizations of membranes in contact with electrolyte solutions*, no. Aphys 2003. Woodhead Publishing Limited, 2005. doi: 10.1016/B978-008044648-6.50074-4.

[35] A. Nechache, M. Cassir, and A. Ringuedé, "Solid oxide electrolysis cell analysis by means of electrochemical impedance spectroscopy: A review," *Journal of Power Sources*, vol. 258, pp. 164–181, 2014, doi: 10.1016/j.jpowsour.2014.01.110.

[36] S. E. Wolf *et al.*, "Boundary Investigation of High-Temperature Co-Electrolysis Towards Direct CO_2 Electrolysis," *J. Electrochem. Soc.*, vol. 169, no. 3, p. 034531, Mar. 2022, doi: 10.1149/1945-7111/ac5e45.

[37] P. Caliandro, A. Nakajo, S. Diethelm, and J. Van Herle, "Model-assisted identification of solid oxide cell elementary processes by electrochemical impedance spectroscopy measurements," *Journal of Power Sources*, vol. 436, p. 226838, Oct. 2019, doi: 10.1016/j.jpowsour.2019.226838.

[38] A. Leonide, "SOFC Modelling and Parameter Identification by means of Impedance Spectroscopy".

[39] A. Bertei, G. Arcolini, J. P. Ouweltjes, Z. Wuillemin, P. Piccardo, and C. Nicolella, "PHYSICALLY-BASED DECONVOLUTION OF IMPEDANCE SPECTRA: INTERPRETATION, FITTING AND VALIDATION OF A NUMERICAL MODEL FOR LANTHANUM STRONTIUM COBALT FERRITE-BASED SOLID OXIDE FUEL CELLS," *Electrochimica Acta*, vol. 208, pp. 129–141, Aug. 2016, doi: 10.1016/j.electacta.2016.04.181.

[40] M. R. Singh, C. Xiang, and N. S. Lewis, "Evaluation of flow schemes for near-neutral pH electrolytes in solar-fuel generators," *Sustainable Energy Fuels*, vol. 1, no. 3, pp. 458–466, 2017, doi: 10.1039/C7SE00062F.

[41] M. R. Singh, C. Xiang, and N. S. Lewis, "Evaluation of flow schemes for near-neutral pH electrolytes in solar-fuel generators," *Sustainable Energy Fuels*, vol. 1, no. 3, pp. 458–466, 2017, doi: 10.1039/C7SE00062F.